The effect of power-density distribution on weld pool behaviour during laser welding

Tim Donders
4560787

Bachelor Thesis
TU Delft

Delft, May 25, 2020
Responsible supervisor:
S. Kenjeres
Daily supervisor:
A. Ebrahimi

The effect of power-density distribution on weld pool behaviour during laser welding

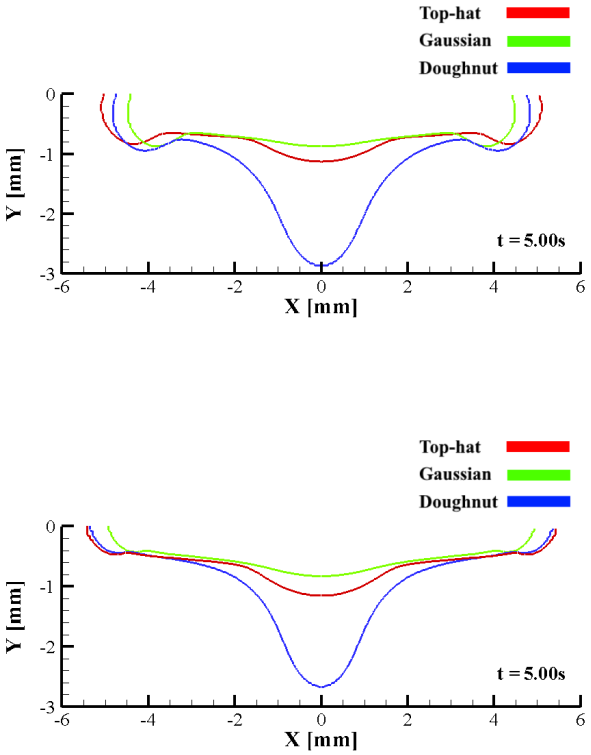

Bachelor Thesis
TU Delft

Delft, May 25, 2020

Abstract

Welding is an extensively used technology by different industries such as aerospace, automotive and marine industry. Welding involves the temporal melting of materials in order to join them together. The quality of the weld is known to depend on the fluid flow and heat transfer in the material. A way to influence the heat transfer and fluid flow, and thus the quality of the weld, is by using different power-density distributions. However, the current literature falls short when combining the different power-density distributions with weld pool behaviour. The aim of this thesis is to study the effects of laser power-density distribution on heat and fluid flow in molten metal melting pools. This will be done by running weld pool simulations using a 2D axisymmetric, flat surface model. These simulations use a top-hat, Gaussian or doughnut laser power-density distribution. Besides, the cases have been simulated for a 20 ppm and a 150 ppm sulfur concentration. That the sulfur concentration has an influence on the weld pool shape was already shown in previous studies. However, it was not known how much the influence of sulfur concentrations varied for different laser power-density distributions.

The laser power-density distributions are found to have a significant influence on the weld pool shape. The doughnut power-density distribution created a three times deeper weld pool than the Gaussian and top-hat power-density distribution. The maximum temperature of the weld pool was also influenced by the power-density distribution. In the case with a sulfur concentration of 20 ppm a discrepancy of 1000 K has been found between the Gaussian and doughnut distribution.

The influence of sulfur concentrations varied for different laser power-density distributions. This influence of the sulfur concentrations has been measured through the difference in aspect ratio for different sulfur concentration cases. For both the top-hat and Gaussian power-density distribution, the aspect ratio differed 0.02 when using a 20 ppm versus a 150 ppm sulfur concentrations. The doughnut power-density distribution reached a higher difference in aspect ratio of 0.1 when using a 20 ppm versus a 150 ppm sulfur concentrations.

The use of different power-density distributions in weld pool simulations results in different weld pool behaviour. Besides, the combination of different sulfur concentrations with power-density distributions largely influenced shape, temperature and fluid flow of the weld pool, which results in a great variation of weld pool shapes and sizes. Because there are different requirements for different welding cases, these results are useful in order to construct a quality weld.

Contents

1. Introduction

1.1 Background

Laser welding is a welding technology that allows for opportunities which are difficult or even impossible to achieve via other welding methods such as Arc welding and gas welding. Laser welding differs from other welding techniques both in equipment and process operation standpoints [1]. Since the discovery of laser welding many studies have been done as it is used widely in different industries such as aerospace, automotive and marine industry. An example of the utility of laser welding is the application on the Audi A4/Q5 doors, here laser welding is used in order to create a maximum viewing angle, which is good for both safety and comfort [2]. Besides these advantages there is also an additional potential for the reduction of the weight of a car. This has been applied to the door of the Audi A6, by reducing the structural single parts, which was possible due to the use of laser welding, the new door concept saved 10kg in weight. These examples show that laser welding is a very useful welding technique, but there is still a lot of room for improvement, especially in the simulation of laser processes [2].
Since the eighties the welding research obtained an important tool called numerical simulation. This allowed for the rapid increase of knowledge and understanding regarding weld pools. The studies done so far have had many different spear points. Some studies focus on a translating heat source (*e.g.* [3, 4]), while others focus on the so called spot-welding (*e.g.* [5]).

Studies regarding weld pool behavior and laser density distributions have been done numerically (*e.g.* [6, 7]) and experimentally (*e.g.* [8, 9]). A few studies even combine the experiments with the numerical models (*e.g.* [10]). The main disadvantage of an experimental study on weld pools is the high temperatures, small dimensions and lack of transparency of the weld pool. The application of different laser density distributions is relatively new for weld pools. In this paper a look will be taken at the effect of the various laser density distributions on the weld pool behaviour. The main focus in this paper is on the numerical simulation of hydrodynamics and heat transfer in a weld pool for different laser density distributions.

1.2 Scope

The main goal of the present work is understand the effects of different laser power-density distributions on low-Prandtl number melting pools. To achieve this goal, the following research question is defined.
What are the effects of laser power-density distribution on heat and fluid flow in molten metal melting pools?

1.3 Outline

This bachelor thesis is organized as follows. The literature review is done in chapter 2. This chapter shows the reason why this study is done. The focus of the literature is mostly on heat transfer, fluid flow and laser density distributions. Chapter 3 discusses two physical models which will be used for numerical simulation. In chapter 4 the solution procedure is discussed. Chapter 5 reports the numerical simulations done. Finally the concluding remarks of this report will be made in chapter 6.

2. Literature review

This chapter reviews the state-of-the-art of weld pools and laser power-density distributions. Here is discussed what we already know regarding these subjects, what is missing in the literature and what are the limitations. In the end, it is discussed how this thesis contributes to the advancement of the field.

2.1 Overview on weld pool flow studies

Studies on the development of weld pools have been carried out for a few decades now, both by experiments and numerical simulation. This section gives an overview of experimental techniques and numerical models. All these researches are based upon understanding the physics which involve the hydrodynamics and heat transfer of the weld pool. The foundation of these physics have been formed by DebRoy and David [11] and Lancaster [12]. Weld pool hydrodynamics are dominated by Marangoni convection due to surface tension gradients. These hydrodynamics play a substantial role in the heat transfer to the surrounding heat affected zone. The heat transfer affects among others: the final weld shape, post solidification micro-structures, and residual stresses, which correlate to the weld quality [13]. The dependence of surface tension on temperature and element concentration results in a significant spatial variation of surface tension, which is manifested in Marangoni stresses at the free surface. Marangoni stresses are balanced by shear stresses due to the liquid metal viscosity. The weld pool flow is essentially driven by differences in surface tension. This is called the Marangoni driven flow and it can have a profound impact on the final weld shapes [14].

2.1.1 Experimental studies

There have been many experimental studies on weld pool flows. Most of these studies faced the same obstacles, which are: small dimensions, high temperatures and the lack of transparency [4]. Nevertheless, several successful measurements of weld pool free surface velocities have been reported [8]. This is done by following the movement of oxide particles which are transported by the surface flow [15–17].

Lately, more advanced techniques have been used that can deal with the lack of transparency. For example X-ray transmission, has been used in order to measure the internal flow velocities. This technique has been used by Mizutani et al. [18], Naito et al. [19], Katayama et al. [20] and it solved the transparency problem regarding liquid metal.

2.1.2 Numerical modelling

Numerical modelling has been of great importance to the advancement of the field of weld pool hydrodynamics [21]. An advantage of numerical models is that it does not have any problems with small dimensions, high temperatures and the lack of transparency. Numerical modellings allows for an extensive analysis regarding the time-dependent fluid flow and heat transfer, both at free surface and inside the weld pool. This section reviews the available models with attention to several aspects, such as free surface deformation, surface active elements, enhancement factors and solidification stage.

Many researches have relied on the flat surface assumption. The researches vary in complexity regarding e.g. dimensionality: 2D [22, 23], 2D axisymmetric [24] and 3D [25–27]. Other researches allowed for surface deformation, Paul and Debroy [28] showed that free surface simulations were found to be in fair agreement with the corresponding experimental values. Thompson and Szekely [29] used a coordinate transformation in order to investigate the transport phenomena in weld pools with surface deformation, providing an accurate model for describing the conditions at the free surface and calculating the surface tension forces.

In the research of Sahoo et al. [30] a mathematical model was created. This model showed the influence of a surface active element (*e.g.* sulfur) and temperature on the surface tension. Which is still the most used model for simulating surface tension.

Some researches used enhancement factors for thermal conductivity and viscosity in order to fit numerical data to experimental observations [24, 25]. The reasoning behind using enhancement factors is to enhance the momentum and heat transfer due to the flow instabilities and/or possibly turbulence. The use of enhancement factors can lead to inaccurate predictions of the time-dependent mixing of the elements in the weld pool. Which is important for the determination of the micro structure quality [13].

Most numerical models do not take the solidification phase into account. The problem with this is that experimental results were obtained for solidified welds, but numerical results showed welds at the end of the heating stage. However there are some works out there which have included this solidification phase in their simulations. A few examples are: Chen et al. [3], Saldi et al. [21], Paul and Debroy [28], Pavlyk and Dilthey [31], Xu et al. [32] and Han and Liou [26]. Saldi et al. [21] shows that the weld pool shape significantly changes after the heat source has been switched off. During the cool down phase is even possible that the surface tension gradient switches from negative to positive. Resulting in the Marangoni flow direction to change from outward to inward, which deepens the weld pool up to 30%. Pavlyk and Dilthey [31] showed the coupling between macro-scale flow and heat simulation with solidification at micro-structure scale.

2.2 Studies on power-density distributions

Studies on non-standard laser power-density distributions are still pretty new, but interest in the subject has been growing rapidly due to having a lot of applications [33]. Duocastella and Arnold [33] wrote a review on the knowledge of Bessel and annular (doughnut) beams, they showed the advantages/disadvantages of using different power-density distributions and the applications these beams can be used for.

Important to the advancement of the field was the research of Han and Liou [26]. In this research a numerical study was done regarding the effect of different laser beam modes on the development of a melt pool. They showed that the use of different power-density distributions has a significant influence on the weld pool and thus on the product quality. However there is still quite a lot of work to be done regarding the effect of various power-density distributions on melt pools.

There is already a lot of knowledge about the standard power-density distributions which are the Gaussian and top-hat power-density distribution. These power-density distributions have been used in most of the numerical weld pool models [24, 32]. There are two different ways to add the top-hat power-density distribution in a simulation. The first one is by the approximation of an uniform power-density profile as is done by Xu et al. [32], the other technique is by the use of a Super-Gaussian beam as has been done by Wu et al. [34].

It is possible to create different beams via beam shaping. With beam shaping it is possible to create C-shaped, triangular, rectangular and diamond beams instead of the standard circular beams [33, 35–37]. Sundqvist et al. [35] showed that beam shaping results in different weld pool shapes. Whereas, Sheikh and Li [37] showed that non-conventional laser beam geometries can be effectively employed for laser processes such as surface heating, transformation hardening, forming, melting of metallic materials, and laser cutting.

2.3 Concluding remarks

As already shown in the literature, there is a already a lot of research done regarding the heat transfer and fluid flow inside a low-Prandtl number melting pool. However, the used models still have limitations. There is already a lot known about various laser power-density distributions, even though this is still a new research subject. However, most of the research is focused on beam shaping. The current literature falls short when combining the different power-density distributions with weld pool behaviour. Due to the fact that the application of different laser density distributions is relatively new for weld pools. This thesis is focused on the numerical simulation of the heat transfer and fluid flow inside a weld pool by various power-density distributions. This will be combined with different surface active element concentrations as there is little to no research about the combination of various laser power-density distributions with different surface active element concentrations. It is important to do research regarding the effect of various power-density distributions on weld pool behaviour as it could help by increasing the quality of different welds. As for various welding cases there are different requirements in order to construct a quality weld.

3. Methodology

This chapter presents the methodology regarding the numerical simulation of weld pools using various laser density distributions. The methodology narrows the topic down, as welding pool behaviour is a really broad subject. It focuses mainly on heat transfer and fluid flow in a weld pool. Besides, various laser power-density distributions are discussed, the relevant dimensionless constants are given and a simple sketch of the problem is provided. The methodology also touches upon the difference between 2D and 3D modelling.

3.1 Simple sketch of the problem

The present study takes a look at the influence of different power-density distributions on the weld pool shape, fluid flow and heat transfer in the weld pool. Figure 3.1 gives a sketch of the cross section of a weld pool.

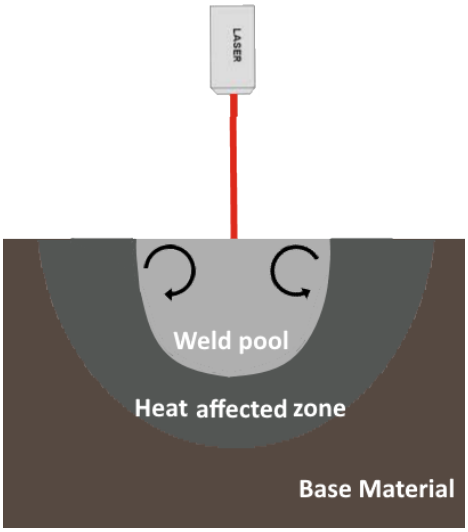

Figure 3.1: Sketch of the cross section of the material, showing the general concept of the weld pool, heat affected zone and the base material in which the effect of heat transfer of the laser is assumed to be negligible.

The solid material is heated by a laser source, after some time the melting temperature of the material is reached. The material in the weld pool is now molten and its heat effects an area around

it. In the base material it is assumed that the heat transfer is negligible [4].

3.2 Various laser power-density distributions

Gaussian density profiles and top-hat profiles are density profiles that are used by most commercial lasers providers, but in the last few years a lot of different power-density distributions for lasers have been used [33]. This paper takes a look at why different power-density distributions are used and what effect these power-density distributions could have on a weld pool. Figure 3.2 shows the power-density distributions which are used in this thesis.

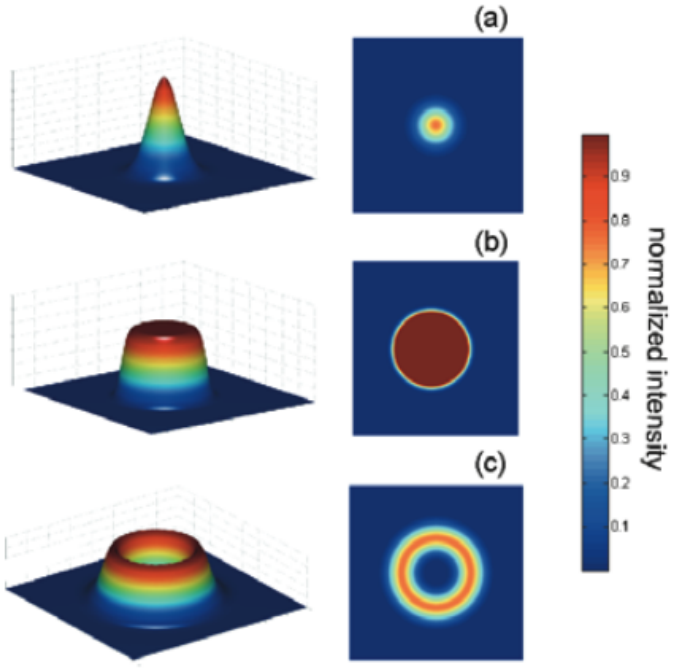

Figure 3.2: 2D and 3D power-density distributions of (a) Gaussian beam, (b) Top-hat beam and (c) Doughnut beam. Adapted from "Bessel and annular beams for materials processing" by Duocastella M. and Arnold C.B., 2012, Laser and photonics reviews, 6, p. 608. Reprinted with permission.

The Gaussian and top-hat power-density distribution are chosen because these power-density distributions are used a lot as already mentioned above. The doughnut power-density distribution is used because the sideways spreading of the heated area is bigger than that of a Gaussian or even top-hat beam, while at the same time the maximum temperature rise is lower in the center, due to the null power-density on-axis [33].

3.2.1 Gaussian power-density distribution

The Gaussian power-density distribution, shown in figure 3.2a, is the most common beam shape and thus is generally seen as the standard beam shape. This is due to the fact that the Fourier transform is also Gaussian, thus its shape is preserved [38]. The preserved shape is very useful as

the laser beam keeps the same shape while passing through lenses. When using a Gaussian beam as power-density distribution for creating a weld pool with a low, 20 ppm, sulfur concentration, it is expected to create a deep welding pool [32]. For the intensity of a Gaussian laser beam the so called TEM_{00} mode is used, as that mode satisfies a Gaussian power-density distribution [26]. The intensity profile is given by [27]:

$$I_G(x,y,z) = \frac{2P_{\text{laser}}}{\pi R_w(z)^2} e^{-2\left(\frac{r}{R_w(z)}\right)^2}, \tag{3.1}$$

where, P_{laser} is the laser power, R_w the radius of the beams waist at depth z and r is the distance from the computational cell to the laser beam center, r is a polar coordinate which can also be written as: $r = \sqrt{(x-x_0)^2 + (y-y_0)^2}$. The expansion of the laser beam relative to the z-axis is given by:

$$R_w(z) = R_0 \sqrt{1 + (\frac{zM\lambda}{\pi R_0^2})^2}, \tag{3.2}$$

where, R_0 is the radius of the focused laser beam, λ the wavelength of the laser and M the beam quality factor, which is 1 for an ideal Gaussian beam. In this paper it is assumed that the beam is ideal and the laser is close to the material, which means that the second term in the square root is really small. This is the reason this term is neglected, which allows for the use of $R_w = R_0$.

3.2.2 Top-hat beams

There a few different ways to approximate a top-hat power-density distribution: via a super Gaussian power-density distribution, flattened-Gaussian power-density distribution or via an uniform power-density distribution. A super-Gaussian function can be used in order to define the power-density distribution of a top-hat beam. This is given by [39]:

$$I_{SG}(x,y,z) = Ae^{-2\left(\frac{r}{R_w(z)}\right)^a}, \tag{3.3}$$

where, A is the maximum for the intensity of the super-Gaussian(SG) function and a the SG power. This SG function reduces to a Gaussian function for $a = 2$. The equation 3.3 can be rewritten by combining this with equation 3.1, in order to obtain an expression for A:

$$I_{SG}(x,y,z) = \frac{2P_{\text{laser}}}{\pi R_w(z)^a} e^{-2\left(\frac{r}{R_w(z)}\right)^a}. \tag{3.4}$$

When taking $a \to \infty$ the function tends to a rectangle, which would be the ideal top-hat function. The disadvantage of using this power-density distribution is that it is difficult to handle analytically. Because of this the so called flattened-Gaussian profiles are used, which are easier to solve analytically [40].

In the models in this paper it is assumed that the top-hat beam is ideal, which means that the power-density distribution profile is uniform. This is done because a well-made top-hat beam is close to an uniform beam, hence there is no big difference in the simulation [33].

3.2.3 Doughnut power-density distribution

The doughnut power-density distribution, also called the annular power-density distribution has no intensity in the center, as is shown in figure 3.2c. Such a beam can be created by using destructive interference on a Gaussian laser beam. The intensity of a doughnut shaped beam is given by equation 3.5. Using the relation that was found by Yoo et al. [9]: $R_p = 0.75R_w(z)$ the following formula is obtained.

$$I_D(x,y,z) = \frac{16P_{\text{laser}}}{9\pi R_w(z)^2}\left(\frac{4r}{3R_w(z)}\right)^2 e^{-\left(\frac{4r}{3R_w(z)}\right)^2}. \tag{3.5}$$

Again it is assumed that the laser is close to the material and the beam quality factor M is assumed to be 1. Resulting in the assumption that $R_w = R_0$.

Keep in mind that there are many different ways to create an Annular beam, as the only requirement for an Annular beam is that there is no power distributed in its center. It is for example possible to create rectangular or triangular Annular beams. This is done through beam shaping, which is not examined in this thesis.

3.3 Relevant physical phenomena

The laser is only able to supply a heat influx to the surface of the material, which sets into effect a heat transfer inside the material. This means that there will be temperature gradients, these temperature gradients over the melt pool surface result in a spatial variation of surface tension [13]. Liquid flows from zones of low surface tension to zones with high surface tension. This mechanism is called the Marangoni effect and it is given significance by the thermal Marangoni number. The Marangoni number compares the rate at which thermal energy is transported through the Marangoni flow to the rate at which thermal energy diffuses [11, 41]. The Marangoni number is given by:

$$\text{Ma} = \frac{\frac{\partial\sigma}{\partial T}L\Delta T}{\mu\alpha}, \tag{3.6}$$

where, $\frac{\partial\sigma}{\partial T}$ is the variation in surface tension due to the temperature, L a characteristic length scale, ΔT the temperature difference, μ the dynamic viscosity and α the thermal diffusity.

The temperature gradient in the weld pool also causes density gradients, which induces a buoyancy force. The buoyancy-driven flow can be described by the Rayleigh number, which is a product of the dimensionless Grashof and Prandtl numbers. The Rayleigh number gives the ratio between the inertia forces and surface tension forces [42].

$$\text{Ra} = \frac{\rho^2 g\beta\Delta T L^3}{\mu^2}\frac{\mu}{\rho\alpha} = \frac{\rho g\beta\Delta T L^3}{\mu\alpha}, \tag{3.7}$$

where, ρ is the density of the fluid, g the gravitational acceleration and β the thermal expansion coefficient. In order to determine which effect dominates the fluid flow in the weld pool, the dynamic Bond number is determined. The dynamic Bond number (eq. 3.8) gives the ration between the

Rayleigh number over the Marangoni number, which gives the ratio of the gravitational force over surface tension force.

$$\mathrm{Bo} = \frac{\mathrm{Ra}}{\mathrm{Ma}} = \frac{\rho g \beta \Delta T L^2}{\frac{\partial \sigma}{\partial T} \Delta T}. \tag{3.8}$$

For a spot weld pool using stainless steel, the Bond number is typically between 10^{-4}-10^{-3} [13]. The Bond number represents the ratio between the buoyancy force and the Marangoni effect, therefore it can be concluded that the buoyancy driven flow can be neglected for a spot weld pool using stainless steel. This assumption is tested in section 6.4.1.

In a weld pool there are two ways for heat transport. The first one is convection and the second is conduction or diffusion. In order to find which of these two is the primary drive of heat transfer in a weld pool the Péclet number for heat transfer is calculated in equation 3.10. The Péclet number gives the ratio between heat transport by convection over heat transport by conduction [43]. But first an expression for the characteristic velocity should be found using:

$$U = \frac{\Delta \sigma}{\mu} \simeq \frac{\frac{\partial \sigma}{\partial T} \Delta T}{\mu}, \tag{3.9}$$

where, U is the characteristic velocity and $\Delta\sigma$ the difference in surface tension. This expression is used in order to define equation 3.10.

$$\mathrm{Pe}_{\mathrm{heat}} = \frac{UL}{\alpha} \simeq \frac{\frac{\partial \sigma}{\partial T} \Delta T L}{\alpha \mu}. \tag{3.10}$$

For weld pools the Péclet number is in the order of 10-10^2 [13]. This indicates that heat transport by convection is more significant than the conductive and diffusive heat transport.

Whether the fluid flow in the weld pool is laminar or turbulent is determined by the Reynolds number, which determines the ratio between inertia forces and viscous forces. In the present model the inertia forces are given by the surface tension forces. The Reynolds number can be rewritten using equation 3.9 in order to obtain:

$$\mathrm{Re} = \frac{U \rho L}{\mu} \simeq \frac{\frac{\partial \sigma}{\partial T} \Delta T \rho L}{\mu^2}, \tag{3.11}$$

whether the weld pool flow is laminar or turbulent is still an unresolved issue [13]. For a spot weld pool the Reynolds number can get as large as 10^5, which creates a highly unstable free surface flow. This has been observed experimentally by Zhao et al. [8]. Aboutalebi et al. [44] suggested that weld pool flow becomes turbulent if the Reynolds number is much larger than 100.

3.4 Heat transfer in a weld pool

3.4.1 Conservation of energy

The heat transfer inside a weld pool should be discussed in order to understand development of a weld pool. The energy conservation equation at atmospheric pressure is given by [45]:

$$\frac{\partial(\rho H)}{\partial t} + \nabla \cdot (\rho H \mathbf{U}) = -(\nabla \cdot q) - (\tau : \nabla \mathbf{U}), \tag{3.12}$$

where, H the enthalpy and $\mathbf{U}$ the velocity vector. Fourier's law is used to rewrite $-(\nabla \cdot q)$ to $\nabla \cdot (k \nabla T)$ [45]. The viscous velocity term, $-(\tau : \nabla \mathbf{U})$, is neglected as it is only of significance for enormous gradients in the velocity. The conservation of energy can be rewritten to equation 3.13. This is done through the use of the assumptions above and through including a source term for the latent heat change and surface heat, the last one is neglected if the flat surface assumption is used.

$$\frac{\partial(\rho C_p T)}{\partial t} + \nabla(\rho C_p \mathbf{U} T) = \nabla \cdot (k \nabla T) + S_T, \tag{3.13}$$

where, ρ is the density of the liquid metal, C_p the specific heat, k the thermal conductivity, S_T the energy source term which is analysed in section 4.1.3 .

3.4.2 Heat flux

The total heat flux is determined by calculating the sum of the ingoing and outgoing flux.

$$q"_{total} = q"_{in} - q"_{out} = q"_{laser} - q"_{conv} - q"_{rad}, \tag{3.14}$$

where, $q"_{laser}$ is the heat from the laser, $q"_{conv}$ the heat loss from convection and $q"_{rad}$ the heat emitted due to radiation. $q"_{laser}, q"_{rad}$ and $q"_{conv}$ can be obtained by the following equations 3.15 - 3.17.

$$q"_{laser} = \mathcal{A} I \delta_s, \tag{3.15}$$

$$q"_{conv} = h_c(T - T_\infty), \tag{3.16}$$

$$q"_{rad} = \epsilon \sigma (T^4 - T_\infty^4), \tag{3.17}$$

where, $\mathcal{A}$ is the absorption coefficient which is material specific, $I(x, y)$ the intensity of the incident laser beam, δ_s the delta Dirac function which peaks at the surface and decays away from it. This makes sure that the energy of the laser only acts on the surface, h_c the convective heat transfer coefficient, ϵ the emissivity of the material, T_∞ the temperature around the object [26]. The intensity of the laser varies for various power-density distributions. These were already analysed in section 3.2. Sharir et al. [46] stated that the heat loss through convection is small in comparison to the heat loss via radiation, especially for high temperatures. Therefore the heat loss through convection will be neglected in the present model. Natural convection is the primary drive for heat transfer, as already discussed in section 3.3. Heat transfer through conduction will be largest at the surface which is directly irradiated by the laser [47].

3.5 Fluid flow

3.5.1 Conservation of mass and momentum

To analyse fluid flow inside a weld pool, the continuity equation and the conservation of momentum are defined as [26, 48]:

$$\frac{\partial}{\partial t}\rho + \nabla \cdot (\rho \mathbf{U}) = 0 \tag{3.18}$$

$$\frac{\partial}{\partial t}(\rho \mathbf{U}) + \nabla \cdot (\rho \mathbf{U}\mathbf{U}) = \nabla \cdot (\mu \nabla \mathbf{U}) - \nabla p + \mathbf{S_U}, \tag{3.19}$$

where, μ is the dynamic viscosity, $\mathbf{S_U}$ the momentum source term which is analysed in section 4.1.2.

3.5.2 The mushy zone

For non pure materials there is a so called mushy zone. This is the range between the solidus temperature T_s and the liquidus temperature T_l. In this mushy zone the material is partly solid and partly liquid. The liquid volume fraction f_l is used to determine how liquid the mushy zone is [10].

$$f_l = \begin{cases} 0, & 0 < T < T_s. \\ \dfrac{T - T_s}{T_l - T_s}, & T_s < T < T_l \\ 1, & T > T_l \end{cases} \tag{3.20}$$

The liquid volume fraction is zero in the solid part and one in the liquid part of the material. This mushy zone also defines a condition which the welding pool system has to meet. This condition being the zero velocity condition inside the solid. The mushy zone allows the velocity to decrease gradually from a certain value inside the liquid, to a lower value inside the mushy zone and in the end to be equal to zero in the solid. This is done by the use of Darcy's law, which will be discussed in section 4.1.2.

3.5.3 The Marangoni effect

Temperature gradients over the melt pool surface induce a spatial variation in surface tension. This gradient leads to the Marangoni force which is balanced by viscous forces [48]. This is called the shear stress and it can be used in order to determine the gradient of the velocity vector.

$$\tau_{f \to w} = \frac{\partial \sigma}{\partial m} = \mu \frac{\partial U}{\partial n}, \tag{3.21}$$

where, $\tau_{f \to w}$ is the shear stress of the fluid on the wall, n and m are tangential vectors. The shear stress can also be written as the spatial variation in surface tension $\dfrac{\partial \sigma}{\partial m}$. As made clear in section 3.3 the surface tension is also dependent on the temperature, and the temperature again has a spatial dependency. This means that the shear stress can be rewritten to [36]:

$$\frac{\partial \sigma}{\partial T}\frac{\partial T}{\partial m} = \mu \frac{\partial U}{\partial n}, \tag{3.22}$$

the surface tension still has to be defined in order to be able to use equation 3.22. For the surface tension the model proposed by Sahoo et al. [30] is used. The surface tension is given by [10]:

$$\sigma = -\sigma_{\text{pure,m}} + \frac{\partial \sigma_{pure}}{\partial T}(T - T_m) - RT\Gamma_s ln(1 + k_l a_i e^{-\frac{\Delta H_{\text{pure}}}{RT}}), \tag{3.23}$$

where, $\sigma_{\text{pure,m}}$ is the surface tension of a pure material at its melting point, $\dfrac{\partial \sigma_{pure}}{\partial T}$ the variation in the surface tension of a pure material due to the temperature, which is assumed constant [30], R the universal gas constant, Γ the surface excess at saturation, k_l a constant corresponding to

the segregation entropy, a_i the activity of material i (depends on sulfur concentration), ΔH_{pure} the standard heat of adsorption. Equation 3.23 is derived with respect to T in order to obtain the variation in surface tension with temperature. Using the adsorption coefficient $K = k_l e^{-\frac{\Delta H_{\text{pure}}}{RT}}$. The following equation can be obtained:

$$\frac{\partial \sigma}{\partial T} = \frac{\partial \sigma_{pure}}{\partial T} - R\Gamma_s ln(1 + Ka_i) - \frac{\Gamma_s K a_i \Delta H_{\text{pure}}}{(1 + Ka_i)T}. \tag{3.24}$$

Marangoni flow direction

The model for the variation in surface tension with temperature, shown in equation 3.24, can give rise to different $\frac{\partial \sigma}{\partial T}$ coefficients, $\frac{\partial \sigma}{\partial T}$ can be positive or negative, this largely depends on the amount of sulfur inside the weld pool [13]. For low concentrations of sulfur the surface tension decreases when the temperature increases. Fluids always flow from places of low surface tension to places with high surface tension, so an outward flow will take place in this case. For high concentrations of sulfur the surface tension increases when the temperature increases. This creates an inward flow. There is one special case, where the surface tension increases with the temperature but from a certain temperature onward the surface tension decreases with the temperature. This creates radially inward and outward vortices in the weld pool, figure 3.3c. These vortices create a complex fluid flow inside the weld pool [24]. This change of sign for the $\frac{\partial \sigma}{\partial T}$ coefficient happens at the critical temperature. Figure 3.3 gives a schematic representation of these phenomena for a Gaussian power-density distribution.

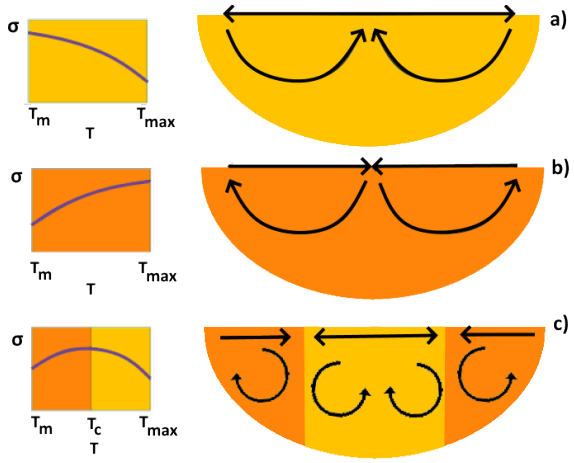

Figure 3.3: Sketch of the cross section of the flow inside a weld pool for different $\frac{\partial \sigma}{\partial T}$ coefficients. With T_m being the melting temperature, T_{max} the maximum temperature and T_c the critical temperature. The laser is using a Gaussian density distribution profile.

Currently there is not much research about the effect of different power-density distributions on the fluid flow in the weld pool. By using different power-density distribution functions the shape of the weld pool will change. This thesis will take a detailed look at the effect of a various power-density

distributions on the fluid flows inside the weld pool. For the doughnut power-density distribution, see figure 3.2, there will be two T_{max} peaks. This results in twice as many vortices in the weld pool. Resulting in a more turbulent fluid flow inside the weld pool. It also has a relatively low temperature in the center of the welding pool, due to the zero intensity on-axis [33]. A schematic sketch of the Marangoni flow inside a weld pool using an Annular beam is given in figure 3.4.

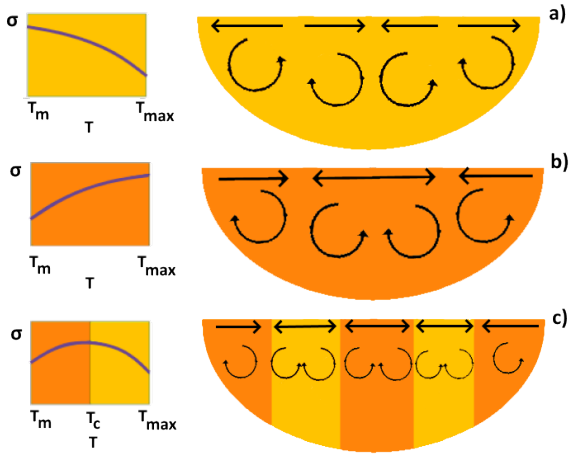

Figure 3.4: Sketch of the cross section of the flow inside a weld pool for different $\frac{\partial \sigma}{\partial T}$ coefficients. The laser is using a doughnut power-density distribution profile.

The top-hat profile does not have any extra vortices in comparison to the Gaussian profile. However the area which is at the maximum temperature in the weld pool is relatively high. This would mean in case of a critical temperature (fig. 3.3c), the (orange) part, below the critical temperature will be considerably smaller than the (yellow) part, above the critical temperature. This will have the effect that the vortices meet closer to the side of the weld pool than that they do for a Gaussian distribution.
It is important to research the effect of various laser density distributions on weld pool behaviour as it could help to improve the quality of laser welding products.

3.6 2D axisymmetric vs 3D modelling

There are advantages and disadvantages coupled to using a 2D model over a 3D model. The main advantage is the use of a lot less computing power, but this comes at a cost. First of all when using 2D models the capturing of boundary effects has to be given up and instead the stress field will be estimated in a zone where stationary conditions arise during welding [49]. It has been discovered that 2D and 3D models match better when the thermal conductivity of a material is lower, this is possible using enhancement factors, and if the welding speed is higher [49, 50]. To conclude, when using 2D weld pool models the accuracy of the model becomes worse, but it requires a lot less computing power.

4. The physical model

In this thesis a physical model with the flat-surface assumption is used to describe the creation of a weld pool. This model is called the solid-liquid model, which will be discussed in detail in section 4.1.

4.1 Solid-liquid model

4.1.1 Relevant equations

The solid-liquid model is based on the continuum equation (eq. 4.1), the equations for the conservation of momentum (eq. 4.2) and energy (eq. 4.3).

$$\frac{\partial}{\partial t}\rho + \nabla \cdot (\rho \mathbf{U}) = 0 \tag{4.1}$$

$$\frac{\partial}{\partial t}(\rho \mathbf{U}) + \nabla \cdot (\rho \mathbf{U}\mathbf{U}) = \nabla \cdot (\mu \nabla \mathbf{U}) - \nabla p + \mathbf{S_U} \tag{4.2}$$

$$\frac{\partial(\rho C_p T)}{\partial t} + \nabla(\rho C_p \mathbf{U} T) = \nabla \cdot (k \nabla T) + S_T. \tag{4.3}$$

4.1.2 Momentum source term

The momentum source term consists of two parts $\mathbf{S_U} = \mathbf{S_B} + \mathbf{S_D}$. The first part, S_B, comes from the temperature difference, this creates a density difference, which creates a buoyancy force in the direction of the gravitation field, this contribution is given by:

$$\mathbf{S_B} = \rho \mathbf{g} \beta (T - T_{ref}), \tag{4.4}$$

where, β is the thermal expansion coefficient and T_{ref} the reference temperature. S_D satisfies the following condition: the velocity field is zero in solid regions. The idea is to gradually reduce the velocities from a finite number in the liquid to zero in the full solid [47]. This is called the Darcy damping force (eq. 4.5), which can be derived from the *Kozeny-Carman* equation [32].

$$\mathbf{S_D} = A\mathbf{U} = -C \frac{(1 - f_l)^2}{f_l^3 + b} \mathbf{U}, \tag{4.5}$$

where, A is the drag coefficient for a porous media model in the mushy zone, C a constant describing the mushy zone morphology ($10^6 \sim 10^8$) [51], f_l the liquid volume fraction, (eq. 3.20) and b a small constant ($10^{-4} \sim 10^{-3}$) [51], which is introduced in order to avoid division by zero. Equation 4.4 and 4.5 are used in order to find an expression for $\mathbf{S_U}$:

$$\mathbf{S_U} = \rho \mathbf{g} \beta (T - T_{ref}) - C \frac{(1 - f_l)^2}{f_l^3 + b} \mathbf{U}. \tag{4.6}$$

4.1.3 Energy source term

The energy source term S_T defines the evolution of the latent heat. The latent heat is absorbed when the phase of the material changes from solid to liquid. The inverse is also true. The energy source term is given as [10, 13, 47, 52]:

$$S_T = -\left(\frac{\partial(\rho \Delta H)}{\partial t} + \nabla \cdot (\rho \mathbf{U} \Delta H) \right), \tag{4.7}$$

where, ΔH is the latent heat change, also known as the latent enthalpy change, which is a function depending on temperature. Two cases exist, an isothermal phase change and a non-isothermal phase change. For an isothermal phase change, the latent heat will be zero if the temperature (T) is lower than the melting temperature (T_m). This suddenly changes if $T > T_m$, at that moment latent heat is L. For a non-isothermal phase the change from zero to L will take place during a temperature interval. The range of the temperature interval is from the temperature of the solidus (T_s) to the temperature of the liquidus (T_l). This change of latent heat will be assumed linear in this thesis as that requires less computer power, although in reality this is not a linear line. In order to create a linear line for the latent heat change the energy source term is rewritten to equation 4.8 [52]. Furthermore it is used that the latent heat change $\Delta H = L f_l$ with L being the latent heat of a material [36].

$$S_T = S_P T + S_C \tag{4.8}$$

This is rewritten to [13]:

$$S_T = -\frac{\partial \rho f_l L}{\partial t} = -\rho L \frac{\partial f_l}{\partial T} \frac{\partial T}{\partial t}, \tag{4.9}$$

linking these two equations (4.9 & 4.8) defines the coefficients S_P (eq. 4.10) and S_C (eq. 4.11).

$$S_P = -\frac{\rho L}{\Delta t} \frac{d\mathcal{F}}{dT} \tag{4.10}$$

$$S_C = -S_P \mathcal{F}^{-1} + \frac{\rho L}{\Delta t}(f_l^{old} - f_l) = \frac{\rho L}{\Delta t} \frac{d\mathcal{F}}{dT} \mathcal{F}^{-1} + \frac{\rho L}{\Delta t}(f_l^{old} - f_l) \tag{4.11}$$

Equation 4.10 and 4.11 show that an iteration is taking place between the temperature and the liquid volume fraction. Hereby f_l^{old} references the previous iteration level. In these equations $\mathcal{F}$ is the liquid fraction temperature relationship, meaning that the inverse version $\mathcal{F}^{-1}$ gives a temperature for a certain liquid volume fraction at the old iteration level. In case of a linear profile for f_l between T_s and T_l the inverse liquid temperature relationship $\mathcal{F}^{-1}$ and the differential of the liquid temperature relationship $\dfrac{d\mathcal{F}}{dT}$ are given by equation 4.12 and 4.13:

$$\mathcal{F}^{-1} = \mathcal{F}^{-1}(f_l^{old}) = f_l^{old}(T_l - T_s) + T_s \tag{4.12}$$

$$\frac{d\mathcal{F}}{dT} = \frac{1}{T_l - T_s}. \tag{4.13}$$

4.1.4 Boundary condition

For the solid liquid model the two dependent variables in need of boundary conditions are the temperature and the velocity.

Top surface

In order to define the energy boundary on the top surface, the heat flux balance in equation 4.14 is rewritten as:

$$k\frac{\partial T}{\partial n} = \mathcal{A}I\delta_s - \epsilon\sigma(T^4 - T_\infty^4), \tag{4.14}$$

note that the intensity of the incident laser will be different when using different power-density distributions.

The velocity boundary condition is defined by the shear stress balance, which has been defined in section 3.5.3.

$$\mu\frac{\partial U}{\partial n} = \frac{\partial \sigma}{\partial T}\frac{\partial T}{\partial m} \tag{4.15}$$

Bottom and side surfaces

The temperature boundary condition for the bottom and side surfaces is defined using the assumption that the bottom and side surfaces are adiabatic as this is far away from the weld pool. This means that the gradient of the temperature is zero in other words, the temperature is constant. For the velocity a no-slip condition is assumed. The no-slip condition imposes that at a solid boundary, the fluid will have zero velocity relative to the boundary. So for the bottom and side surface the boundary conditions are: $\frac{\partial T}{\partial n} = 0$ and $\mathbf{U} = \mathbf{0}$.

5. Solution procedure

5.1 General procedure

The numerically solved equations are discussed in this part. It shows the steps to follow in the solution procedure and how the pressure-velocity coupling works.

5.1.1 Computation sequence

The simulations are done using ANSYS 2019 R2 [53]. The computation sequence for the solid-liquid model is shown in a flowchart in figure 5.1. Before the computation processing can start there is a pre-processing phase. In this phase a computational mesh is generated and its quality is evaluated. The evaluation of the quality is extremely important, which will be proven in section 6.1.2. Only a mesh of sufficient quality can lead to an accurate solution [4]. The main computation state starts with applying the initial and boundary conditions to the mesh. In the present model the smeared surface forces and surface heat source are imposed as boundary conditions. The pressure-velocity coupling will be handled using the PISO method [13]. More about this will be explained in section 5.1.2. As mentioned already in section 4.1.3, the liquid fraction and the temperature (and thus the energy equation) depend on each other. Therefore the liquid fraction and the energy equation are solved by the iteration scheme proposed in the same section. During the post-processing, the time-dependent results are processed via field visualisations and plots of variable distributions or time dependencies.

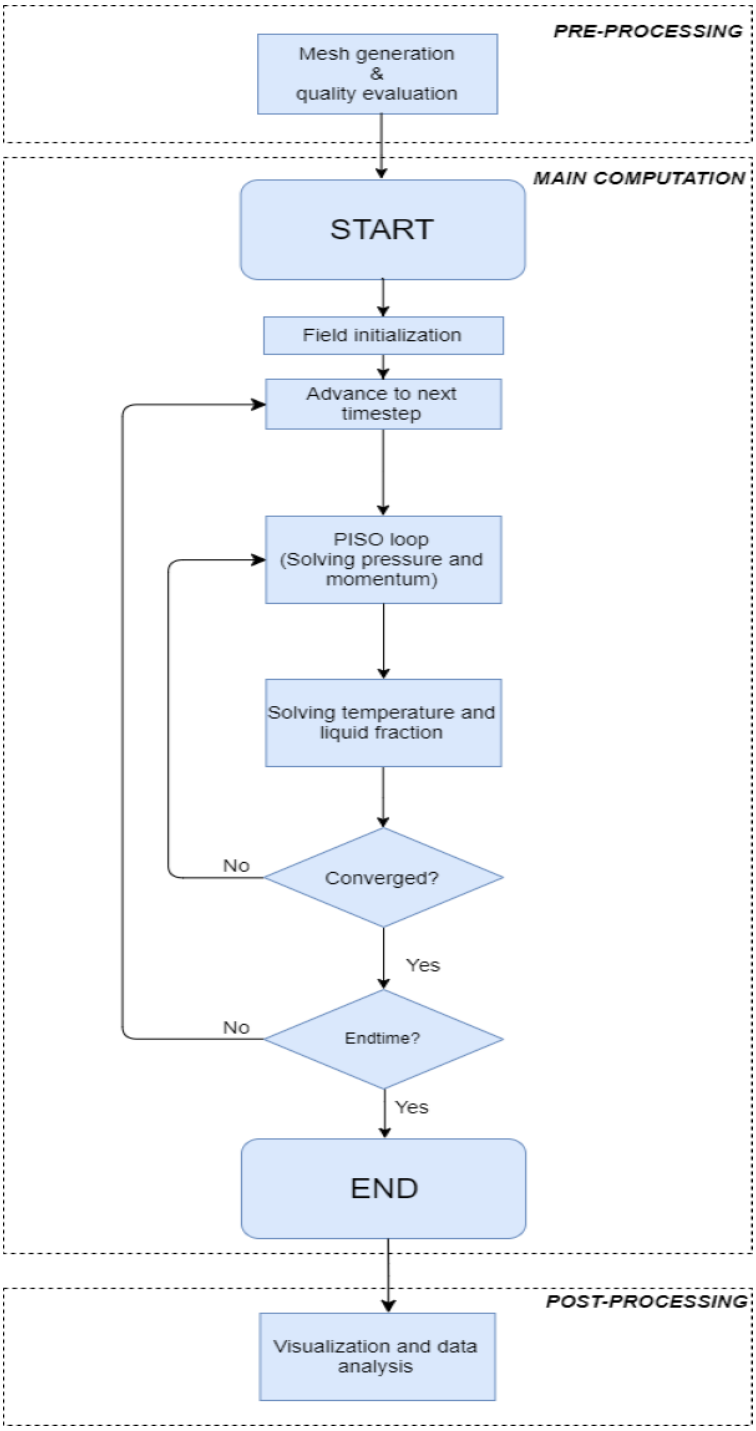

Figure 5.1: Flowchart of the computation sequence of the solid-liquid model.

5.1.2 Pressure-velocity coupling

The momentum equation (eq. 4.2) has a pressure gradient term. In order to solve this momentum equation the pressure distribution needs to be known beforehand. The conservation of mass and momentum are used in order to derive the pressure, which introduces pressure-velocity coupling.
For the solid-liquid model as well the pressure-velocity coupling will be solved using the PISO (Pressure-Implicit with Splitting of Operators) algorithm given by Issa [54]. There are a lot of other solvers which could be used for this operation, like the SIMPLEC (Semi-Implicit Method for Pressure Linked Equations-Consistent) algorithm given by Van Doormaal and Raithby [55]. The PISO algorithm is chosen in the present model as it preforms the momentum corrector step more than once.

The PISO method works as follows [13]:

1. Set the boundary conditions.
2. Solve the discretized momentum equation to compute the guessed velocity field (note: this velocity field does net yet satisfy the continuity).
3. Compute the mass fluxes at the cells faces.
4. Solve the pressure equation.
5. Recalculate the mass fluxes at the cell faces.
6. Recalculate the velocities based on the new pressure field.
7. Update the boundary conditions.
8. Repeat from step 3 for a prescribed number of times.

6. Numerical simulations

This section reports all the numerical simulations done in this paper. First there are a few validation cases, followed by some concluding remarks regarding these cases. Afterwards the 2D axisymmetric numerical simulations done for different laser power-density distributions are reported.

6.1 Validation cases

In order to validate the model used in this paper the following cases:

- 1D Solidification
- 2D Melting phase change
- Role of Sulfur on weld pool behaviour

6.1.1 1D Solidification

The validation case of 1D solidification was reported by Voller and Swaminathan [56], Voller [57]. The case is a 1D slab, made out of an Al-4.5%Cu alloy, which has a transient solidification without convection. The slab has one cold wall ($T_C = 583$K) which is way lower than the solidus temperature ($T_s = 821$K) [50]. The other side wall and the two walls at the top of the slab are considered adiabatic. The initial temperature of the slab ($T_i = 969$K) is higher than the liquidus temperature of ($T_l = 919$K), this means that the slab slowly solidifies in time. Figure 6.1 shows a sketch of the 1D solidification problem, note that the mushy zone is not drawn here, but it does exist.

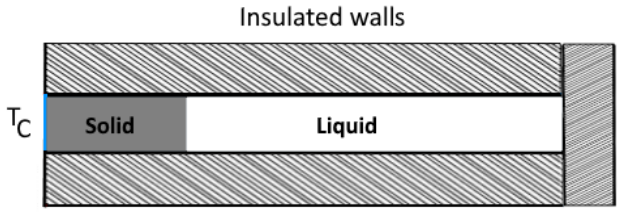

Figure 6.1: Sketch of the solidification process of a 1D slab. There is one cold wall, the other sides are insulated.

The slab has a width of 0.16 m and is made into a mesh of the size 100x1 (as it is 1D). Because this case is in 1D there is no fluid flow and no gravity. The relevant material properties of Al-4.5%Cu are shown in table 6.1 [56].

Table 6.1: A table providing the important material properties of Al-4.5%Cu which are used in the simulation of the 1D solidification case.

Parameter	Symbol	Value	Units
Density solid	ρ_s	2800	$\mathrm{kg/m^3}$
Density liquid	ρ_l	2500	$\mathrm{kg/m^3}$
Specific heat solid	C_{Ps}	900	$\mathrm{J\,kg^{-1}\,K^{-1}}$
Specific heat liquid	C_{Pl}	1100	$\mathrm{J\,kg^{-1}\,K^{-1}}$
Thermal conductivity solid	k_s	200	$\mathrm{W\,m^{-1}\,K^{-1}}$
Thermal conductivity liquid	k_l	90	$\mathrm{W\,m^{-1}\,K^{-1}}$
Latent heat	L	3.9×10^5	$\mathrm{J\,kg^{-1}}$
Initial temperature	T_i	969	K
Liquidus temperature	T_l	919	K
Solidus temperature	T_s	821	K
Cold wall temperature	T_C	573	K
Width	W	0.16	m

For this 1D slab solidification problem simulations where run. Figure **??** shows the development of the solidus and liquidus line over a flow time of 200 s. In this figure the solidus and liquidus line are compared to the semi-analytical data obtained from Voller and Swaminathan [56].

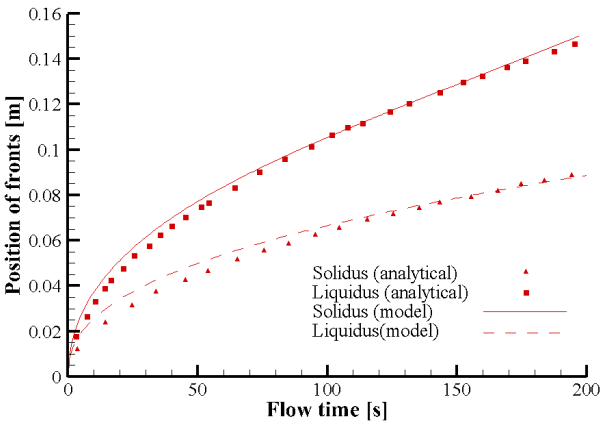

Figure 6.2: Simulation of the solidification of a 1D slab. Comparing the present implementation to the semi-analytical results from Voller and Swaminathan [56].

The left side of the slab slowly starts to become solid while the right side of the slab is still melted. Around the middle portion a mushy zone has established, which is the difference between the liquidus and solidus line. Figure 6.2 shows that the mushy zone grows over the flow time. The results from the present model have been compared to the semi-analytical results from Voller and Swaminathan [56]. From this can be concluded that the present model does slightly overpredict the size of both the liquidus and solidus during the first 100 s of flow times, this overprediction is maximally 4 mm. However the results later after 100 s of flow time show good agreement with the semi-analytical results. In this simulation the temperature gradient is the highest around the mushy

zone, due to the extra energy generated through the phase change. The mushy zone also gets more drawn out by higher flow times, which is as expected.

6.1.2 Melting phase change

The second validation case is a 2D melting phase change case. This case is originally reported by Brent et al. [47]. A solid block of material is heated on one side to a temperature T_H which is above the melting temperature T_m, the other side is heated to T_C which is below T_m. The results will be compared to the model of Saldi [13], who compared his work with the simulation of Brent et al. [47], and the experiments of Gau and Viskanta [58]. For the melting problem gallium is used. The parameters of gallium are the same as Hannoun et al. [59] used. These parameters are provided in table 6.2. A sketch of the problem is given in figure 6.3.

Table 6.2: A table providing the values used in the simulation of the melting phase change of gallium.

Parameter	Symbol	Value	Units
Density	ρ	6.093×10^3	$\mathrm{kg/m^3}$
Specific heat	C_P	381.5	$\mathrm{J\,kg^{-1}\,K^{-1}}$
Thermal conductivity	k	32	$\mathrm{W\,m^{-1}\,K^{-1}}$
Dynamic viscosity	μ	1.81×10^{-3}	$\mathrm{Ns/m^2}$
Thermal expansion coefficient	β	1.20×10^{-4}	$\mathrm{K^{-1}}$
Latent heat	L	8.016×10^4	$\mathrm{J\,kg^{-1}}$
Melting temperature	T_m	302.78	K
Hot wall temperature	T_H	311	K
Cold wall temperature	T_C	301.3	K
Width	W	0.0889	m
Height	H	0.0635	m

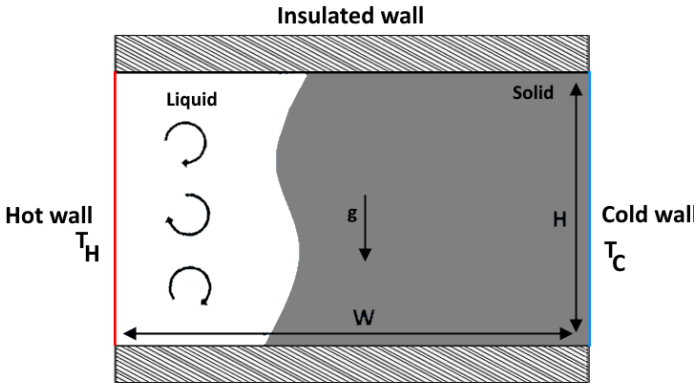

Figure 6.3: Sketch of the melting phase change of gallium.

In order to get an accurate picture the simulation has been run on a 42x32 mesh.

In figure 6.4 the melting front of the plate is shown at various flow times: 2 min, 6 min, 15 min and 19 min. The results of the used model have been compared to the experimental results of Gau and Viskanta [58] and the simulation of Saldi [13].

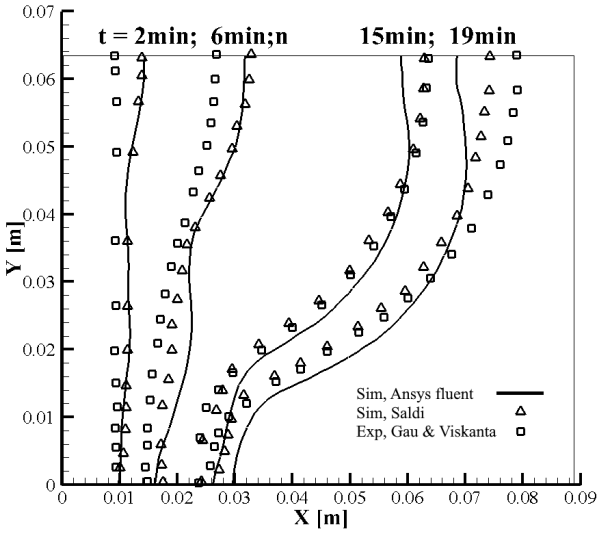

Figure 6.4: Simulation of the melting of a 2D plate. This figure shows the melting front at different flow times.

Figure 6.4 shows that the present Ansys fluent solution shows good agreement with the simulation of Saldi [13], ANSYS® [53]. However, the top part of the melting front is slightly underpredicted , around 5 mm, at 15 min and 19 min. The melting front obtained in the experiment propagates slower in the beginning and faster at later times, the difference between the experimental results and the present simulation is 1 cm. Figure 6.4 shows that the present simulation slightly overpredicts the bottom side of the melting front while slightly underpredicting the top side of the melting front.

The same simulation has been run on a 100x100 mesh in order to determine the mesh dependency of the solution. This simulation was only run for a flow time of 5 min due to time constraints.

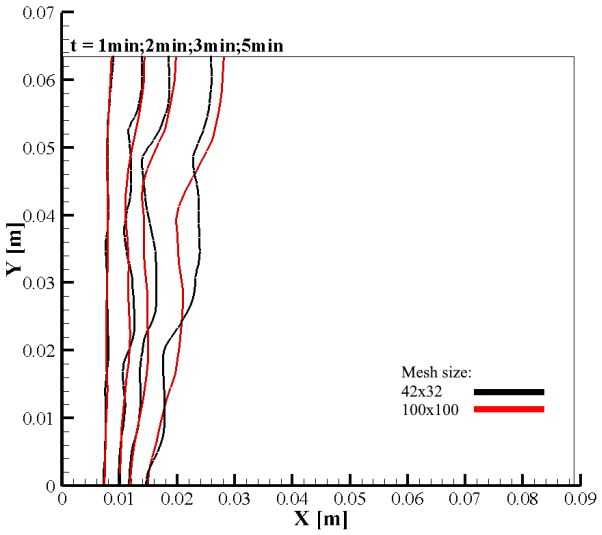

Figure 6.5: Simulation of the melting of a 2D plate. This figure shows the melting front of both the 100x100 and 42x32 mesh at different flow times.

The figure shows that the solution for higher flow times depends significantly on the mesh resolution. At a flow time of 1 min and 3 min the solutions still show similarities, but at a flow time of 5 min the melting front starts to have a different shape. The difference between the two meshes is maximally 4 mm, which will most likely grow for even higher flow times. Therefore it is concluded that the mesh quality has a significant influence on the simulation.

6.1.3 Role of sulfur on weld pool behaviour

The temperature coefficient of surface tension for pure metals is negative. The presence of sulfur in the weld pool can change the temperature coefficient of surface tension to positive. For liquid metals with a positive value for the surface tension gradient, the resulting flow pattern may effect the weld pool shape. The effect on the surface gradient through sulfur has been analyzed by Sahoo et al. [30] which resulted in equation 3.24.

In this validation case, the capability of the present model is evaluated. This is done through the reproduction of the experimental weld pool shapes reported by Pitscheneder et al. [24]. To achieve this, the same set of parameters, see table 6.3, and the same enhancement factors for the viscosity and thermal conductivity are used. The enhancement factor used by Pitscheneder et al. [24] is equal to 7. The experiment simulates the weld pool behaviour of steel for a sulfur concentration of 20 ppm and 150 ppm. In both simulations a laser with a top-hat power-density distribution, a beam radius of 1.4 mm, an absorption coefficient of 0.13 and a laser power of 5200 W is used. Figure 6.6a. shows the shape of the weld pool after a irradiation time of 5 seconds, while using a 20 ppm sulfur concentration. Figure 6.6b. is the only deviant by the use of a 150 ppm sulfur concentration instead of 20 ppm.

Table 6.3: Data used in the simulation regarding the role of sulfur on weld pool behaviour.

Parameter	Symbol	Value	Units
Density	ρ	8.1×10^3	$\mathrm{kg/m^3}$
Specific heat solid	C_{Ps}	620	$\mathrm{J\,kg^{-1}\,K^{-1}}$
Specific heat liquid	C_{Pl}	723.14	$\mathrm{J\,kg^{-1}\,K^{-1}}$
Thermal conductivity solid	k_s	22.9	$\mathrm{W\,m^{-1}\,K^{-1}}$
Thermal conductivity liquid	k_l	160.3	$\mathrm{W\,m^{-1}\,K^{-1}}$
Dynamic viscosity solid	μ_s	6×10^{-3}	$\mathrm{Ns/m^2}$
Dynamic viscosity liquid	μ_l	42×10^{-3}	$\mathrm{Ns/m^2}$
Latent heat	L	250.8×10^3	$\mathrm{J\,kg^{-1}}$
Melting temperature	T_m	1620	K

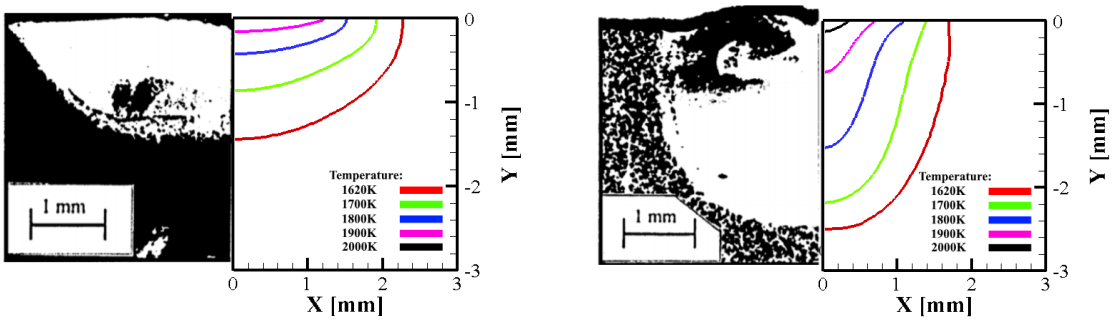

(a) Sulfur concentration of 20 ppm.

(b) Sulfur concentration of 150 ppm

Figure 6.6: The shape of the weld pool after 5 seconds irradiation time using different sulfur concentrations. The left side shows the experimental result obtained from Pitscheneder et al. [24], the right side shows the temperature profiles.

Figure 6.6 shows that the present model preformed well in reproducing the experimental results. Besides, the figure validates that a higher sulfur concentration creates a deep and small weld pool, whilst a smaller sulfur concentration creates a shallow and wide welding pool. This is due to the fact that the sulfur concentration effects the surface tension gradient, which influences the shape of the weld pool.

6.1.4 Concluding remarks

In conclusion, the validation cases are consistent with the literature. The 1D solidification case agrees with the model proposed by Kidess [50], Voller and Swaminathan [56], Voller [57]. However, the first 100 s of flow time slightly overpredicts the solidus and liquidus zones. This overprediction is maximally 4 mm.
The 2D melting phase case is consistent with the case made by Saldi [13]. Besides it is also consistent with the case of Brent et al. [47] and the experimental case of Gau and Viskanta [58]. In the 2D melting phase simulation almost the entire temperature drop is in the liquid region as a lot of energy

gets absorbed during the phase change. The heat transfer inside the plate is dominated by natural convection, especially for higher flow times. This is in agreement with the literature.
The mesh dependency of the solution has been briefly mentioned. It showed that the solution is significantly mesh dependent for higher flow times. This has to be kept in mind while creating the weld pool simulations for various laser power-density distributions.
The role of sulfur on weld pool behaviour has also been analysed. From the simulations conducted it can be concluded that the sulfur concentration has an effect of the surface tension gradient and thus on the weld pool shape. High sulfur concentrations create a small and deep weld pool while small sulfur concentrations create a shallow and wide weld pool. These results are consistent with the experiment conducted by Pitscheneder et al. [24].

6.2 Problem description

This section describes the weld pool simulations. The weld pools are created on a 15 mm by 15 mm 2D axisymmetric disc. In the numerous simulations the laser power-density distribution functions are varied. The laser is centered at the origin and is aimed towards the positive x-direction. The case is axisymmetric around the x-axis.
This work is focused on the grade 304 stainless steel (SS304) which is the most common stainless steel [25]. The properties of SS304 are shown in table 6.4, the properties are taken from Mishra et al. [25], Patel et al. [60], Kraus [61]. The simulations are done using the surface tension gradient proposed by Sahoo et al. [30]. The need for this surface tension gradient has been explained in section 3.5.3, this was validated in section 6.1.3.
The laser that is used has a power of 5200 W and a beam radius of 1.4 mm. The mushy zone constant C is chosen at 10^8 [51].
In the simulations a look is taken at the development of the weld pool up until 5 seconds of irradiation time. During this time the liquid fraction, the temperature distribution, the depth and width of the liquidus, the depth and width of the solidus are monitored. The difference between the values for the liquidus and the solidus is represented by the mushy zone. However, the mushy zone in the simulations will be small, due to the fact that the solidus and liquidus temperature of SS304 are relatively close to each other, $T_{dif} = 40\,\mathrm{K}$. With the depth and width of the weld pool the depth-to-width ratio, also called the aspect ratio, is determined [62]. Note that the depth and width of the weld pool are measured from the origin. There is some heat loss from the weld pool towards the atmosphere via radiation and convection. In section 3.4.2 it was mentioned that the impact of the heat loss from the weld pool through convection is relatively small in comparison to radiation, so only the heat loss through radiation is taken into account during these simulations [46]. The simulations are done in the solid-liquid model. In these cases the buoyancy flow is neglected as its impact is small relative to the Marangoni effect, which is already stated in section 3.3. The simulations for the solid-liquid model will be run once with a sulfur concentration of 150 ppm and once with a sulfur concentration of 20 ppm. For each of the laser power-density distributions a test case has been made where fluid flow is disabled.

Table 6.4: A table providing the important properties of SS304, which is the used material in the weld pool simulations.

Parameter	Symbol	Value	Units
Density	ρ	7200	$\mathrm{kg/m^3}$
Specific heat liquid	C_{Pl}	806.74	$\mathrm{J\,kg^{-1}\,K^{-1}}$
Specific heat solid	C_{Ps}	702.24	$\mathrm{J\,kg^{-1}\,K^{-1}}$
Thermal conductivity	k	25.08	$\mathrm{W\,m^{-1}\,K^{-1}}$
Dynamic viscosity	μ	6.7×10^{-3}	$\mathrm{Ns/m^2}$
Latent heat	L	246×10^3	$\mathrm{J\,kg^{-1}}$
Absorptivity	$\mathcal{A}$	0.27	–
Emissivity	ϵ	0.41	–
Liquidus temperature	T_l	1785	K
Solidus temperature	T_s	1745	K
Width	W	15	mm
Height	H	15	mm

6.3 Simulations without fluid flow

In order to see the influence of fluid flow on the shape of the weld pool, a simulation is run once, for each power-density distribution, without enabling fluid flow. Figure 6.7 shows the simulation of the weld pool shape after an irradiation time of 5 s, using a top-hat, Gaussian and doughnut power-density distribution.

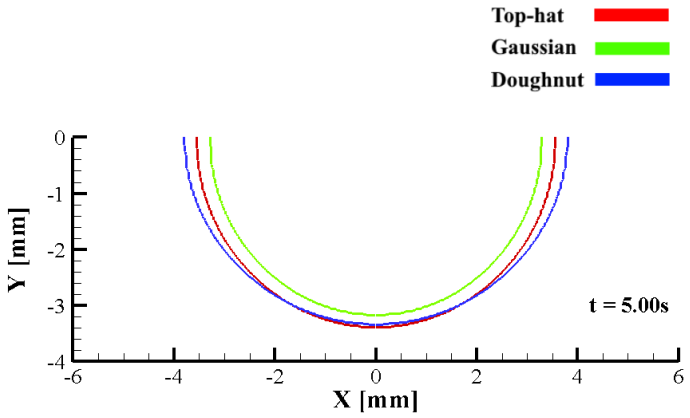

Figure 6.7: Weld pool shapes for different laser power-density distributions. Fluid flow has been disabled.

The figure shows that the weld pools variate in shape, the weld pool shapes variate maximally 0.5 mm in width and 0.15 mm in depth. The doughnut power-density distribution creates the widest weld pool, while the top-hat power-density distribution creates the deepest weld pool. The figure

shows that without fluid flow the melting of SS304 happens really spherically, because all the heat is transferred via conduction.

6.4 Simulations for top-hat power-density distribution

The first simulations have been done using a top-hat laser power-density distribution. For the top-hat profile an uniform density distribution was chosen, which was already discussed in section 3.2.

6.4.1 150 ppm sulfur concentration using solid-liquid model

This simulation was run on the solid-liquid model using a sulfur concentration of 150 ppm. Figure 6.8a shows the fusion lines predicted at different flow times. The surface tension gradient used depends on temperature. In this simulation a sulfur concentration of 150 ppm is used. Figure 6.8a shows that the weld pool primarily expands in its width. This suggests that there is a negative surface tension gradient around the middle of the weld pool, which creates an outward flow. The bulges on the side are created through vortices, which are generated by a positive surface tension gradient. The bulge in the middle is of similar length as the laser radius, which is 1.4 mm. This bulge is created by the two vortices in the middle. Figure 6.8b shows flow streamlines inside the weld pool after 5 s. The fluid flow is directed towards the weld pool edge from the weld pool centre. The figure also shows that the bulges at the sides actually consist out of two different vortices.

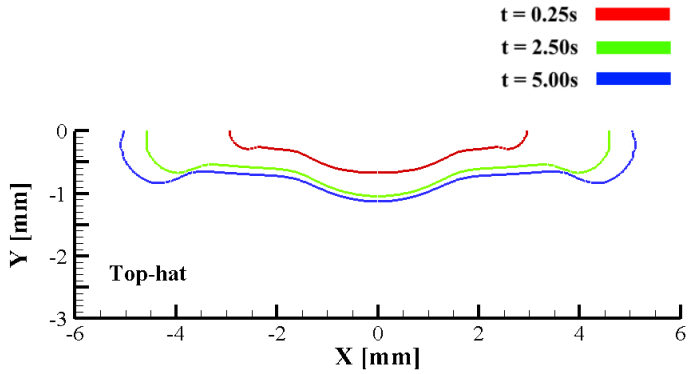

(a) The weld pool shape at different flow times.

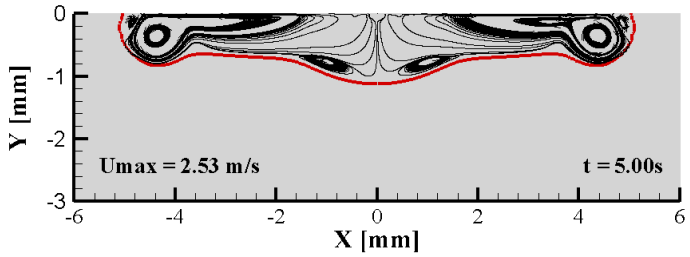

(b) Flow streamlines.

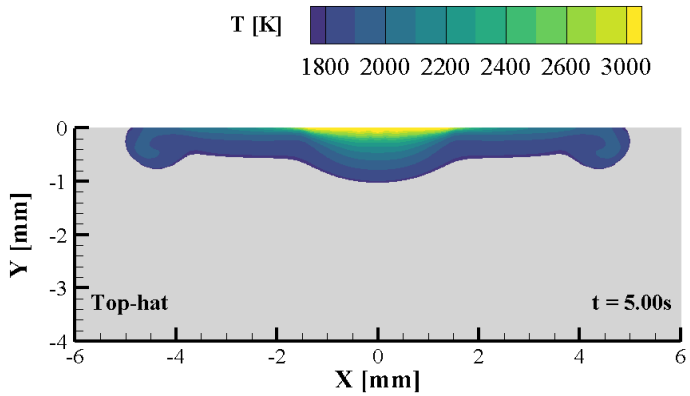

(c) Temperature distribution

Figure 6.8: Simulation of 150 ppm top-hat weld pool.

By using the magnitude of the velocity it is possible to calculate the Péclet number, which is about 225 in this case. This means that the heat transport by convection is 225 times larger than the

heat transport by conduction. Therefore, this proves the statement that the heat transport inside the weld pool is dominated by convection [13].
Figure 6.10 shows the development of the depth and width of the weld pool. The figure shows that the depth of the weld pool quickly stabilizes while the width of the weld pool keeps growing for an extended time period. Besides this the depth-to-width ratio, aspect ratio, is calculated and a graph of this is shown in figure 6.9. The graph shows that the aspect ratio quickly rises to 0.2 and stays quite stable at that point.

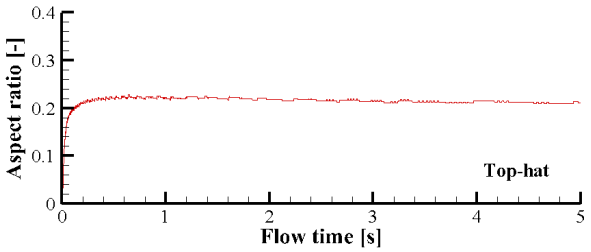

Figure 6.9: The development of the aspect ratio for a top-hat power-density distribution using a sulfur concentration of 150 ppm.

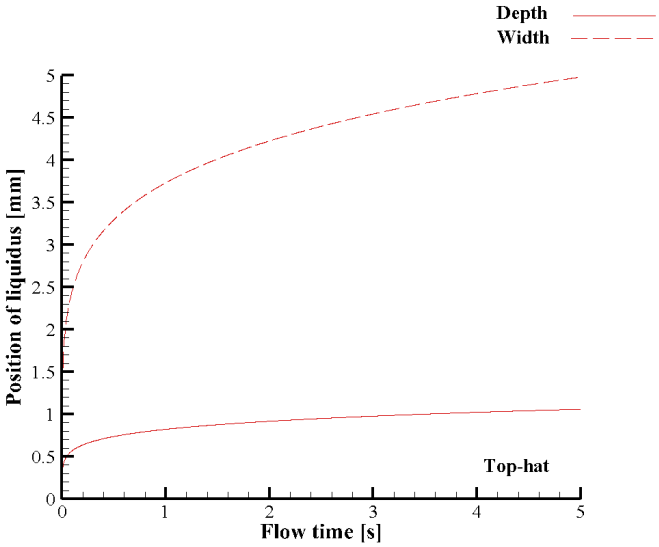

Figure 6.10: The development of the depth and the width of the weld pool when using a top-hat power-density distribution.

Buoyancy force

A simulation with the buoyancy force enabled was run in order to investigate the influence buoyancy force on the development of the weld pool. This simulation used the solid-liquid model, a 150 ppm sulfur concentration and a top-hat power-density distribution. The simulation was done in order to check the assumption to neglect the buoyancy force. Figure 6.11 shows a comparison of the weld pool shape when the buoyancy force is enabled versus when the buoyancy force is disabled.

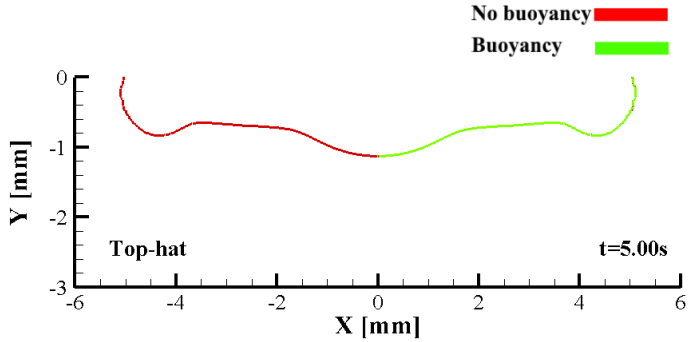

Figure 6.11: The fusion lines for a top-hat power-density distribution. The red line represents the simulation when the buoyancy force is disabled and the green line the one where buoyancy force is enabled. The green contour line is only shown on the right side.

Note that the red line is overlapped by the green line on the right side. In order to compare the results in detail the graph of the development of the width and depth of the liquidus is shown in figure 6.12. Figure 6.12 shows the graphs of the width and depth of the weld pool. In this figure the graphs of the case with and without buoyancy force are shown in the same figure.

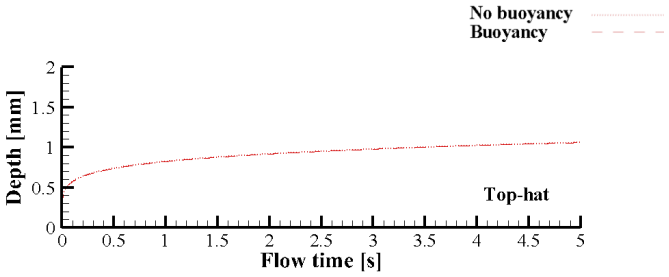

(a) The depth of the weld pool over the flow time.

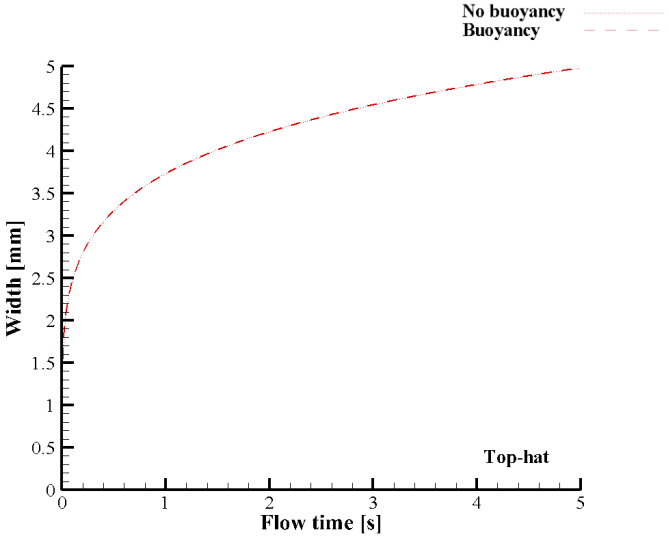

(b) The width of the weld pool over the flow time.

Figure 6.12: Graph showing the development of the depth and the width of the weld pool when using a top-hat power-density distribution.

The figure shows that the graphs for the depth and width are the same when the buoyancy force is enabled/disabled. The data points from both the simulations have been compared in detail in order to find the difference between the two results. This difference between the simulations was maximally 10 µm. In the middle of the weld pool this difference was even smaller, around 100 nm, which is truly negligible. Noteworthy is the fact that the maximum temperature is 100 K lower when buoyancy is enabled. Even though this seems like a significant difference it actually barely effects the weld pool as these only difference maximally 10 µm.

Heat loss through radiation disabled

Another special case was run for the top-hat power-density distribution, disabling the heat loss through radiation was disabled. Figure 6.13 shows the weld pool shape of the case with and without heat loss through radiation.

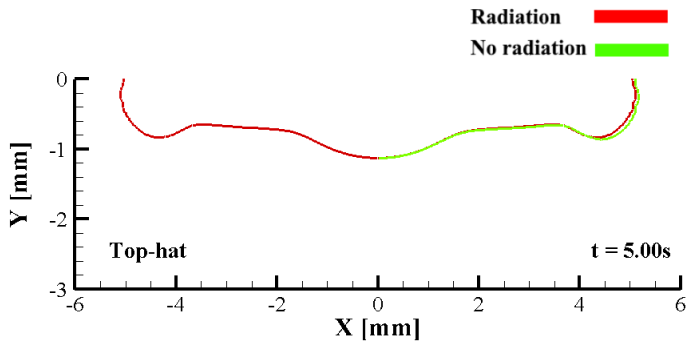

Figure 6.13: The fusion lines for a top-hat power-density distribution. The red line represents the simulation when the heat loss through radiation is enabled and the green line the one where heat loss through radiation is disabled. The green contour line is only shown on the right side.

The figure shows that the weld pool without heat loss through radiation overlaps with the weld pool with heat loss through radiation enabled. The weld pool with radiation enabled is smaller on the side by 60 µm. Figure 6.14 compares the development of the width and depth of the liquidus of the weld pool with and without radiation being enabled.

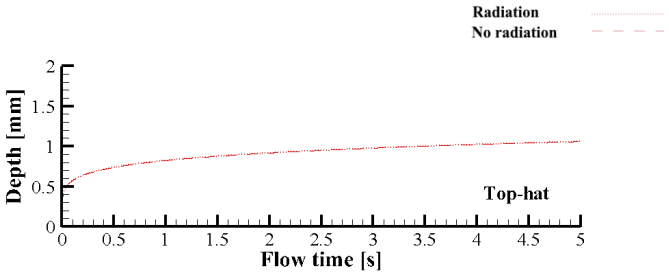

(a) The depth of the liquidus over the flow time.

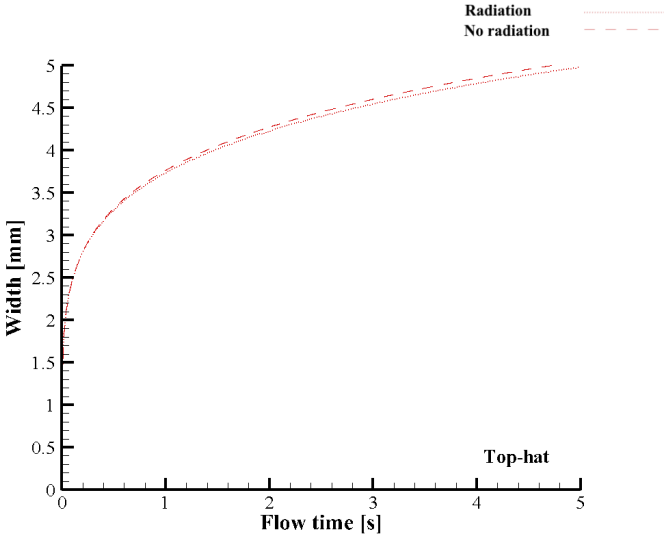

(b) The width of the liquidus over the flow time.

Figure 6.14: Graph showing the development of the depth and the width of the weld pool when using a top-hat power-density distribution. The graph of the case when heat loss through radiation is enabled is shown in the same figure.

As expected the the weld pool without heat loss through radiation is a bit wider, the difference is in the order of 10µm. The difference in the depth of the weld pool is even smaller, around 1 µm, these differences are negligible. Afterwards it was calculated how big the heat losses are in comparison to the heat input from the laser. This calculation showed that the total heat losses are around 2% of the heat input from the laser. Therefore it is concluded that the heat losses could be ignored. However, heat loss through radiation is still used in the present model.

6.4.2 20 ppm sulfur concentration using solid-liquid model

A simulation was run on the solid-liquid model using a top-hat power-density distribution and a sulfur concentration of 20 ppm. Figure 6.15a shows the weld pool shape at different flow times. The figure shows that the weld pool shape does in fact depend on the sulfur concentration. In section 6.1.3 it was shown that a lower sulfur concentration results in a wider weld pool. The weld pool width is 5.33 mm after 5 s versus 4.90 mm when a 150 ppm sulfur concentration is used. Besides this the weld pool is slightly shallower, 0.02 mm, which is a barely notable difference.

Figure 6.15b shows the velocity field inside the weld pool after a radiation time of 5 s. By using the magnitude of the velocity it is possible to calculate the Péclet number, which is about 251 in the 20 ppm sulfur concentration case. This is 26 higher than in the 150 ppm sulfur concentration case, which means that the heat transport by convection is even more important in the 20 ppm sulfur case.

The sulfur concentration also has an influence on the maximum temperature of the weld pool. The maximum temperature of the top-hat weld pool lays 200 K lower when a sulfur concentration of 20 ppm is used instead of a 150 ppm sulfur concentration. Figure 6.15c shows the temperature distribution after 5 s.

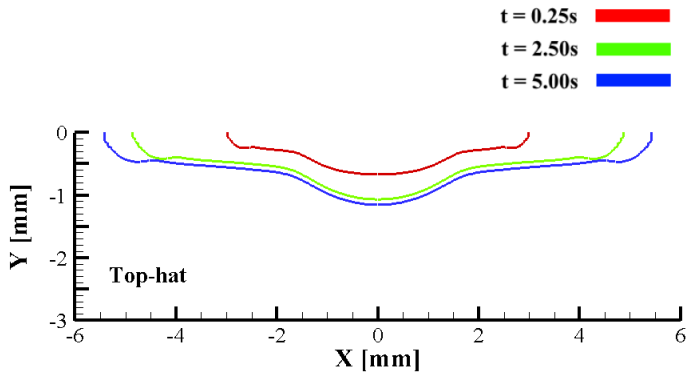

(a) The weld pool shape at different flow times.

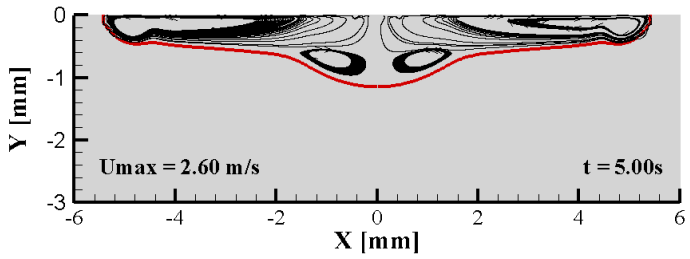

(b) Flow streamlines.

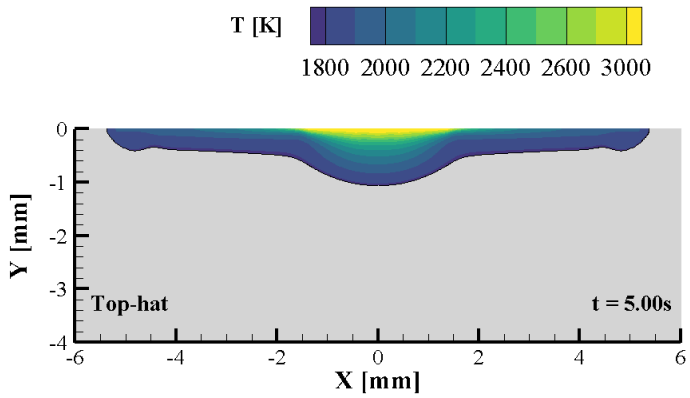

(c) Temperature distribution

Figure 6.15: Simulation of 20 ppm top-hat weld pool.

The development of the depth and width of the weld pool has been monitored, and a graph of this is shown in figure 6.16.

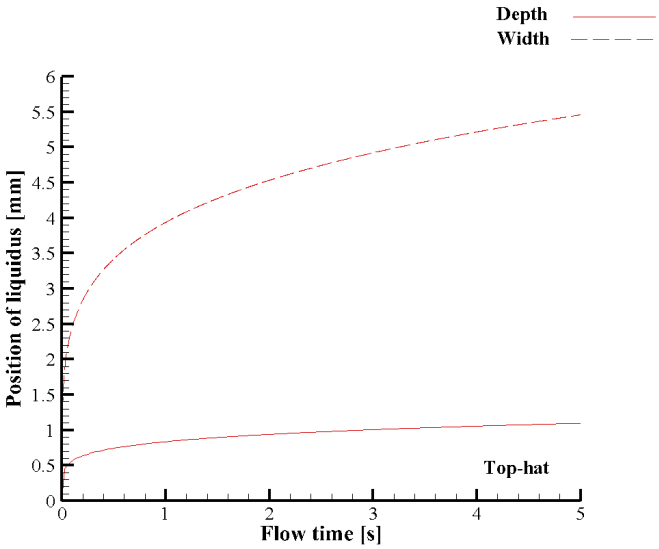

Figure 6.16: Graph showing the development of the depth and the width of the weld pool when using a top-hat power-density distribution.

The aspect ratio is determined for the weld pool and a graph of this is given in figure 6.17.

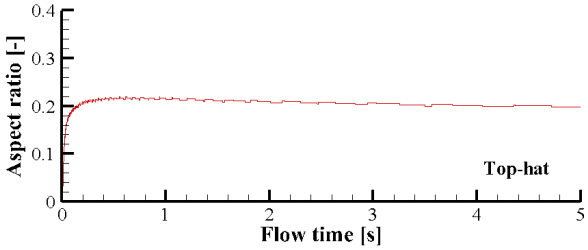

Figure 6.17: Graph showing the development of the aspect ratio for a top-hat power-density distribution using a sulfur concentration of 20 ppm.

The aspect ratio is a slightly, 0.02, lower than the aspect ratio of the 150 ppm case. However, the graph of the depth of the weld pool does not reflect the whole picture of the weld pool shape as the 150 ppm sulfur concentration creates a much deeper weld pool around the sides. But the depth in the middle is almost the same as in the case of the 20 ppm sulfur concentration. Due to the vortices in the middle of the melt pool.

Figure 6.18 compares the weld pool shapes of the 20 ppm and 150 ppm sulfur concentration after 5 s. The sides of the 150 ppm welding pool are significantly deeper for the 20 ppm welding pool, this difference is 0.4 mm at its maximum. This is due to the difference in fluid flow.

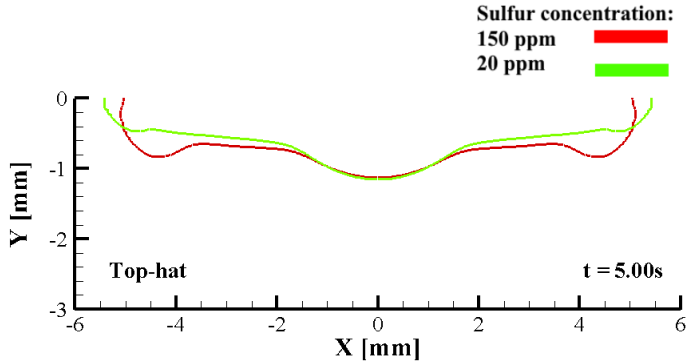

Figure 6.18: The weld pool shape of a 20 and 150 ppm sulfur concentration are compared. In this simulation a top-hat power-density distribution is used to irradiate the material for 5 s

6.5 Simulations for Gaussian power-density distribution

In these simulations the Gaussian laser power-density distribution is used. The power-density distribution is described via equation 3.1.

6.5.1 Solid-liquid model

Figure 6.19a shows the weld pool shape for different flow times. It is notable that the Gaussian weld pool and the top-hat weld pool look similar. This is caused by the fact that the fluid flow for the Gaussian and top-hat power-density distribution are both directed from the center of the weld pool to the edge of the weld pool, as is shown in figure 6.19b. Besides, the sides have double vortices just as is the case for the top-hat weld pool. However, there are quite a few differences in the weld pool shape. The first difference is the bulge in the middle, which is way smaller for the Gaussian power-density distribution than is the case for the top-hat power-density distribution, by 0.3 mm. This is caused by the fact that there are no vortices in the middle for the Gaussian weld pool, as figure 6.19b shows. The Péclet number has been calculated for this case and is equal to 275 in the 150 ppm sulfur concentration case. This is the highest of any of the weld pools, meaning that heat transport through conduction has a very small influence in this case. Figure 6.19c shows the temperature distribution inside the weld pool after 5 s of irradiation time. There is no notable difference between the maximum temperature of the 150 ppm weld pool using a top-hat power-density distribution and a Gaussian power-density distribution.

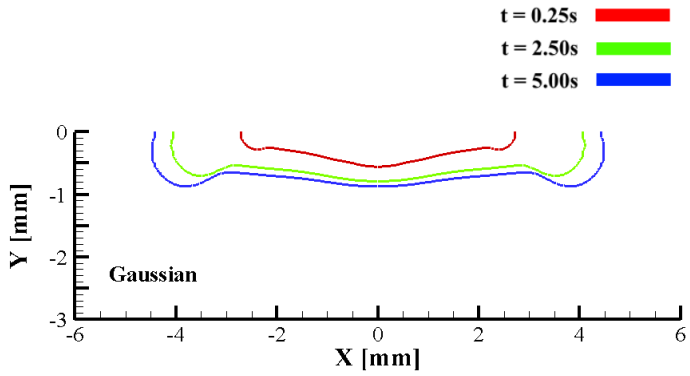

(a) The weld pool shape at different flow times.

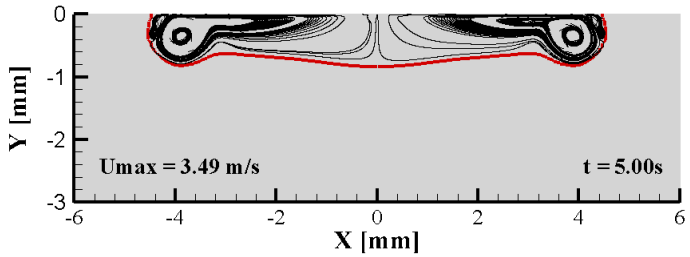

(b) Flow streamlines.

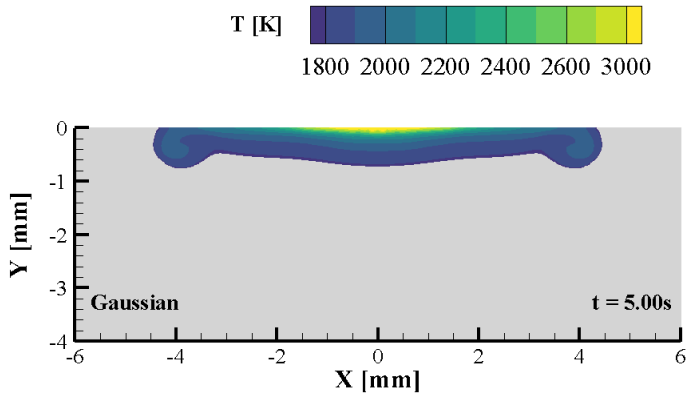

(c) Temperature distribution

Figure 6.19: Simulation of 150 ppm Gaussian weld pool.

There is less heat influx in the material, which effects the whole size of the weld pool. The reason that there is less heat influx is because there is only a small, but high, peak for the Gaussian power-density distribution, while the top-hat power-density distribution is distributed evenly over the radius of the laser, as it is uniform. This results in less heat influx to the material. The fact that there is less heat influx in the material effects the whole size of the weld pool. The weld pool after 5 s is 0.5 mm narrower and 0.3 mm shallower. The development of the Gaussian weld pool is monitored in detail in figure 6.20. In this figure the progress of the width and depth of the weld pool is shown over the flow time. The figure clearly displays the fact that the size of the Gaussian weld pool is smaller than the top-hat weld pool.

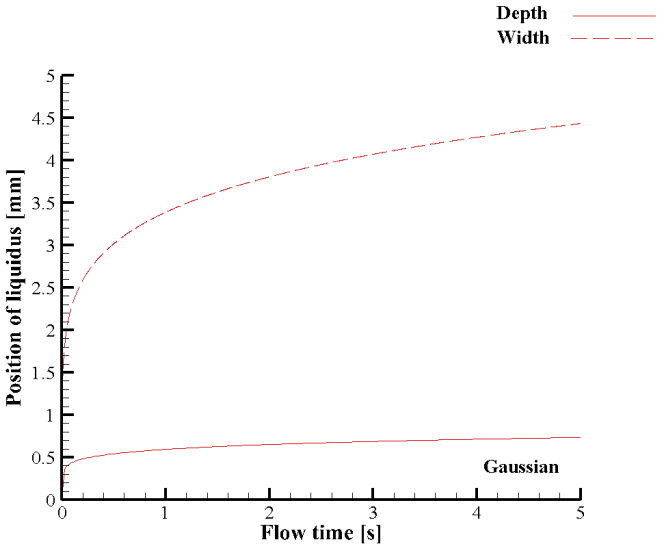

Figure 6.20: Graph showing the development of the depth and the width of the weld pool when using a Gaussian power-density distribution.

The depth-to-width ratio has been calculated, and a graph is shows in figure 6.21.

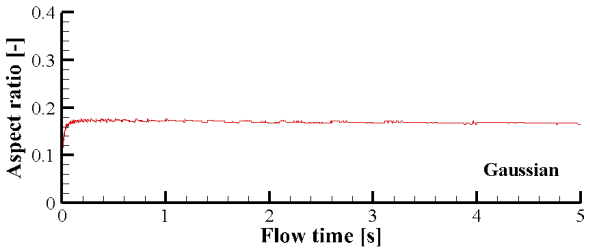

Figure 6.21: Graph showing the development of the aspect ratio for a Gaussian power-density distribution using a sulfur concentration of 150 ppm.

This time the aspect ratio does not hit the 0.2 point, which is expected as the Gaussian weld pool is significantly shallower, as already mentioned above.

6.5.2 20 ppm sulfur concentration using solid-liquid model

The Gaussian power-density distribution is also used in a case with a sulfur concentration of 20 ppm. Figure 6.22a shows the weld pool shape at different flow times.

Figure 6.22b shows the flow streamlines inside the weld pool after an irradiation time of 5 s. The largest difference regarding the 150 ppm and 20 ppm cases is found at the sides of the weld pool. For the 150 ppm Gaussian weld pool double vortices were located at the side, which created the bulges at the side. For the 20 ppm sulfur concentration these double vortices and therefore the bulges at the sides do not exist. The Péclet number for the 20 ppm sulfur concentration case is around 224. Which is significantly lower than in the 150 ppm sulfur concentration case. This is interesting to see because for both the top-hat and doughnut weld pool the Péclet number decreases for higher sulfur concentrations.

The sulfur concentration has an influence on the maximum temperature of the weld pool. The maximum temperature of the Gaussian weld pool lays 150 K higher when a sulfur concentration of 20 ppm is used instead of using a sulfur concentration of 150 ppm. This is really interesting because for both the top-hat and doughnut distribution the maximum temperature is lower when a 20 ppm sulfur concentration is used instead of a 150 ppm sulfur concentration. Figure 6.22c shows the temperature distribution after 5 s.

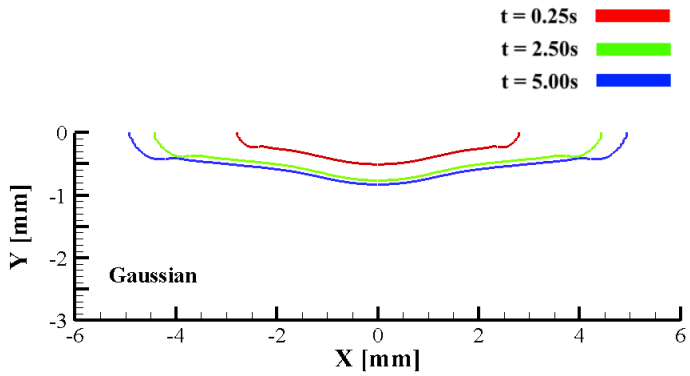

(a) The weld pool shape at different flow times.

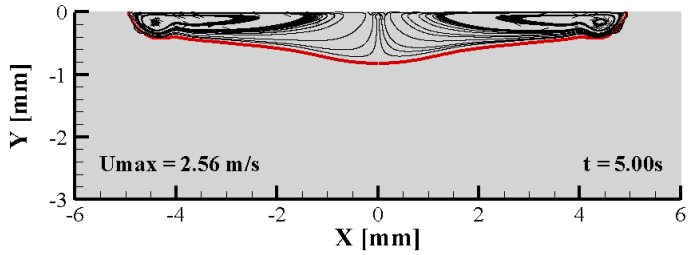

(b) Flow streamlines.

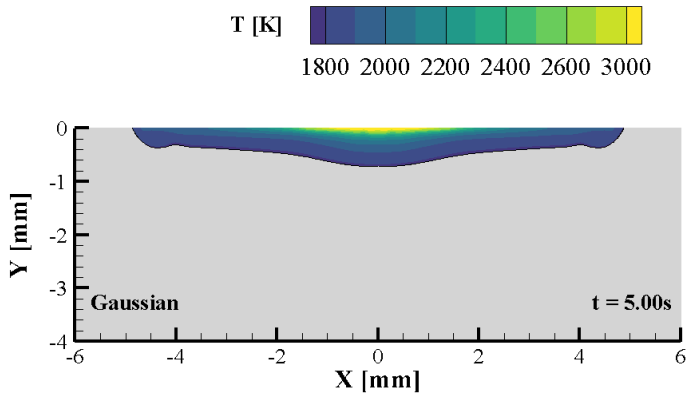

(c) Temperature distribution

Figure 6.22: Simulation of 20 ppm Gaussian weld pool.

In order to compare the weld pool shapes using a sulfur concentration of 20 ppm and 150 ppm figure 6.23 is made. This figure shows clearly that the 20 ppm sulfur concentration creates a wider weld pool compared with the 150 ppm case, which is as expected based on the validation case in section 6.1.3. The weld pool width is 4.84 mm after 5 s versus 4.35 mm when a 150 ppm sulfur concentration is used. The 150 ppm is 0.4 mm deeper at the edges of the weld pool but in the center of the weld pool, where the depth of the weld pool is at its maximum, the two weld pools are the same depth. Figure 6.24 shows the graphs of the development of the width and the depth of the weld pool.

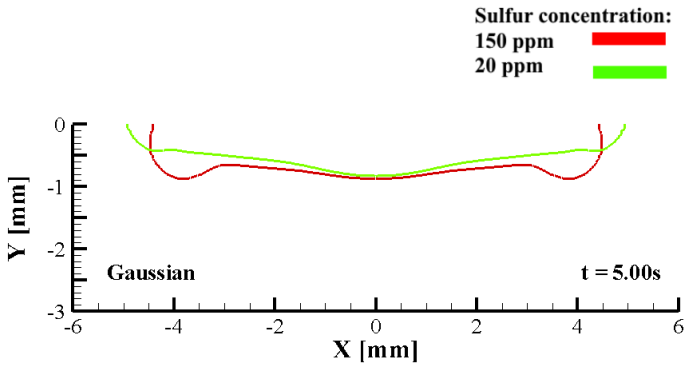

Figure 6.23: The weld pool shape of a 20 and 150 ppm sulfur concentration. In this simulation a Gaussian power-density distribution is used to irradiate the material for 5 s.

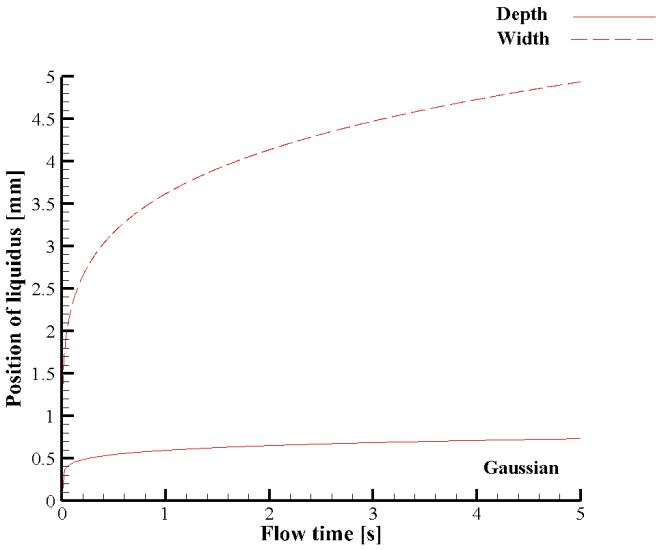

Figure 6.24: The development of the depth and the width of the weld pool when using a Gaussian power-density distribution.

The aspect ratio, is calculated for the 20 ppm weld pool and a graph of this is shown in figure 6.25.

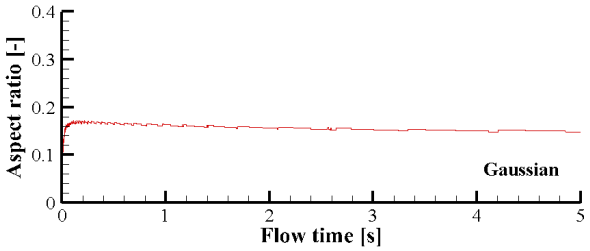

Figure 6.25: Graph showing the development of the aspect ratio for a Gaussian power-density distribution using a sulfur concentration of 20 ppm.

The aspect ratio lays a bit lower, a difference around 0.02, because the Gaussian weld pool with a 20 ppm sulfur concentration is a bit wider then the 150 ppm sulfur concentration, but they have the same depth. The difference in the aspect ratios are the same for the top-hat and Gaussian power-density distribution.

6.6 Simulations for doughnut power-density distribution

These simulations use the doughnut laser power-density distribution, which is described by equation 3.5.

6.6.1 Solid-liquid model

Figure 6.26a shows the weld pool shape while using a doughnut power-density distribution for a flow time of 0.25 s, 2.5 s and 5 s. The original figure is mirrored in order to create a full weld pool, as it is an axisymmetric case. There is a significant difference between shape of the weld pool for the doughnut laser power-density distribution and the shape for other power-density distributions. This is the result of the much more turbulent flow created by a two peak laser.

The fluid flow at work here is shown in figure 6.26b. The magnitude of the velocity is used in order to calculate the Péclet number, which is 92.9 in the 150 ppm sulfur concentration case. This is considerably lower than the Péclet number of both the top-hat (225) and the Gaussian (275) weld pool. From this it is concluded that while the heat transport is still dominated by convection, the influence of the heat transport through conduction is considerably larger in the doughnut weld pool than in the other weld pools. The figure shows that side of the weld pool have the same double vortices as is the case for the 150 ppm Gaussian and top-hat power-density distributions. These vortices create the bulges on the edges of the weld pool, which are 0.1 mm deeper for the doughnut power-density distribution than for the top-hat or Gaussian power-density distribution. The main difference between the power-density distributions is found in the center of the weld pool. For a doughnut power-density distribution, the fluid flow within the laser radius around the origin is directed downwards, which creates a deep weld pool. The fluid flow within the laser radius around the origin is upwards in the case of a Gaussian or top-hat power-density distribution. Another difference is the maximum temperature in the material.

Figure 6.26c shows a zoomed in version of the temperature distribution inside the weld pool. The maximum temperature is 800 K lower while using a doughnut power-density distribution instead of a top-hat or Gaussian power-density distribution. This can be attributed to the fact that the total laser power is divided over two peaks instead of over one peak. From the used power-density distributions it can be derived that the peak of the doughnut power-density distribution is the lowest, hence the lower maximum temperature. This derivation was done by Hannoun et al. [59], who used the same power-density distributions for the doughnut power-density distribution as is used in the present model. Additionally the temperature is distributed more evenly over the y-axis while using the doughnut power-density distribution than in case of the top-hat power-density distribution.

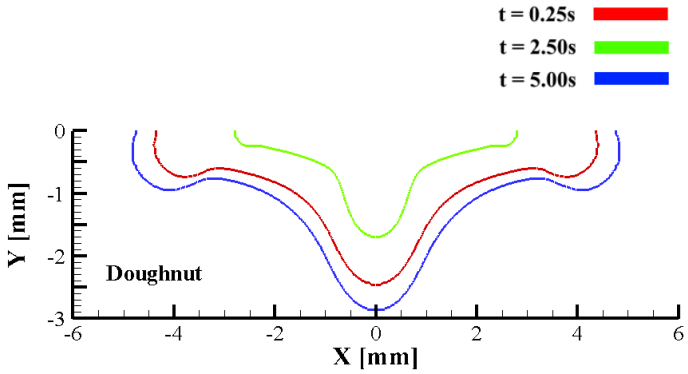

(a) The weld pool shape at different flow times.

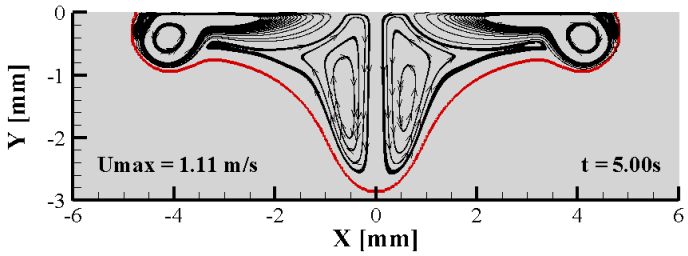

(b) Flow streamlines.

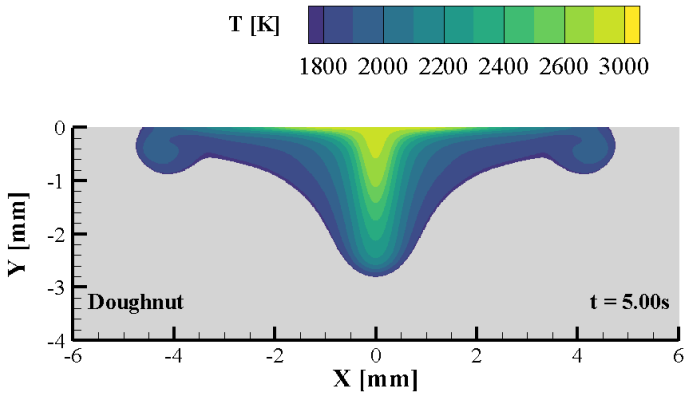

(c) Temperature distribution

Figure 6.26: Simulation of 150 ppm doughnut weld pool.

Beside the temperature, the development of the depth and width of the weld pool were monitored. A graph of this is shown in a graph in figure 6.27.

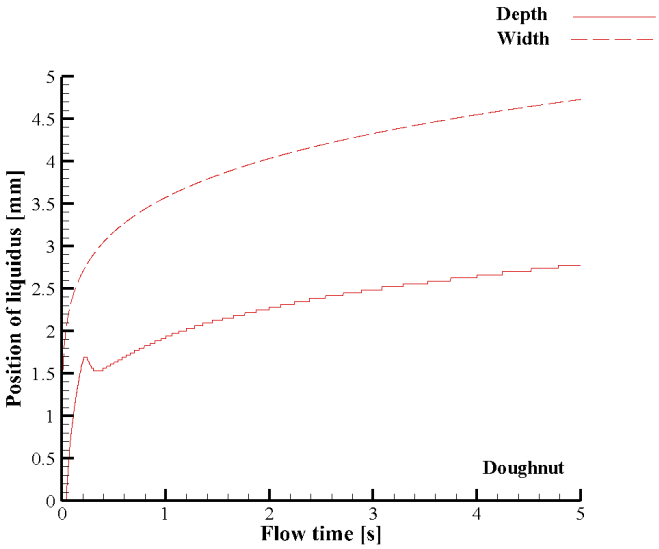

Figure 6.27: The development of the depth and the width of the weld pool when using a doughnut power-density distribution.

From figure 6.27 it can be derived that the doughnut weld pool is slightly smaller than the top-hat weld pool, about 0.3 mm, but also considerably deeper, almost three times as deep. It is noteworthy that the depth of the weld pool drops with 0.15 mm between 0.25 s and 0.5 s. As if yet the reason for this is still unknown, some more research should be done regarding this. The velocity field is directed downwards in the middle which would suggest that the weld pool would develop in depth. For the doughnut weld pool the aspect ratio has been calculated and a graph of it is shown in figure 6.28.

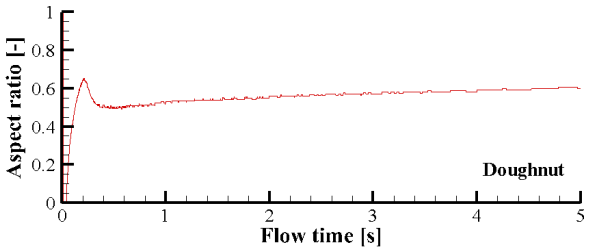

Figure 6.28: The development of the aspect ratio for a doughnut power-density distribution using a sulfur concentration of 150 ppm.

The doughnut weld pool is so much deeper than the Gaussian and top-hat weld pool, while its widths are closer together. This results in a much higher aspect ratio, around 0.6.
Figure 6.29 provides a complete overview of how the weld pool shapes compare to each other. The figure shows that the use of various laser power-density distributions results in different weld pool shapes.

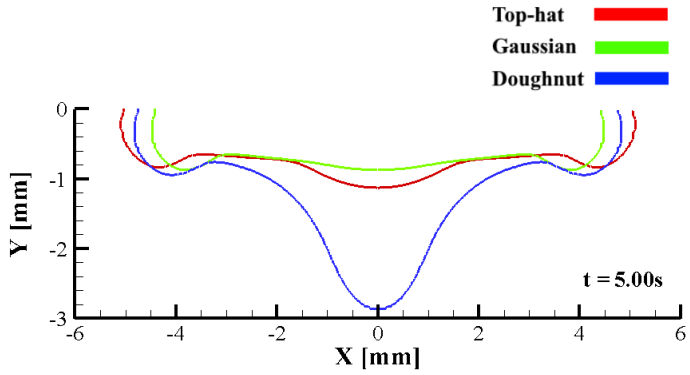

Figure 6.29: The weld pool shape at 5 s, using different laser density distributions.

Figure 6.29 displays the fact that the Gaussian and top-hat weld pools are quite similar, except that the top-hat weld pool is bigger in both width and depth. Besides, the figure shows that the doughnut weld pool has a completely different shape than the Gaussian and top-hat weld pools have.

6.6.2 20 ppm sulfur concentration using solid-liquid model

This section reports the 20 ppm sulfur concentration case using a doughnut power-density distribution. Figure 6.30a shows the development of the weld pool shape. Again the sides of the weld pool are different than in the 150 ppm sulfur concentration case, the maximum difference at the sides is 0.4 mm. The flow streamlines of the 20 ppm sulfur concentration case is shown in figure 6.30b. The figure shows that there is a downward flow in the middle which creates the deep weld pool. Again the edges of the weld pool do not have double vortices and therefore do not have bulges on the side. The Péclet number was calculated, which is 116 in the 20 ppm sulfur concentration case. This is considerably (23.1) higher than in the 150 ppm sulfur concentration case. However, the Péclet number is still significantly lower than the Péclet number of both the top-hat (251) and the Gaussian (224) weld pools using a 20 ppm sulfur concentration.

The sulfur concentration only has a slight influence on the maximum temperature of the weld pool when a doughnut power-density distribution is used. The maximum temperature of the weld pool is 60 K lower for a 20 ppm sulfur concentration. The maximum temperature does not differ as much as in the case of the Gaussian and top-hat power-density distribution, this is caused in essence because the maximum temperature of the doughnut weld pool is considerably lower than in the case of the Gaussian/top-hat weld pool. However this does mean that there is a significant gap, around 1000 K, between the maximum temperature of the 20 ppm doughnut weld pool and the 20 ppm Gaussian weld pool. Figure 6.30c shows the temperature distribution after 5 s.

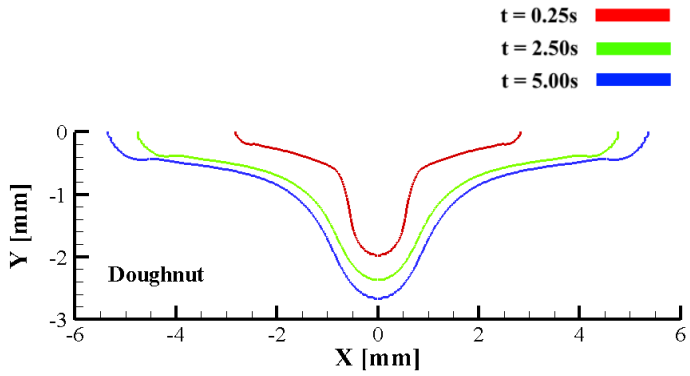

(a) The weld pool shape at different flow times.

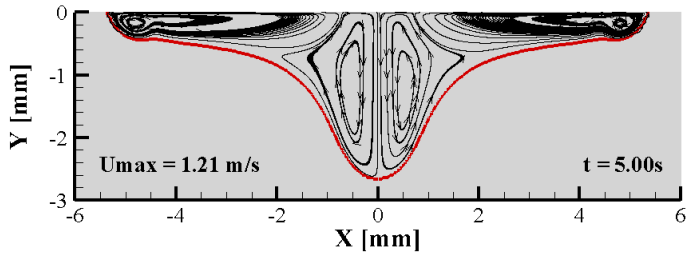

(b) Flow streamlines.

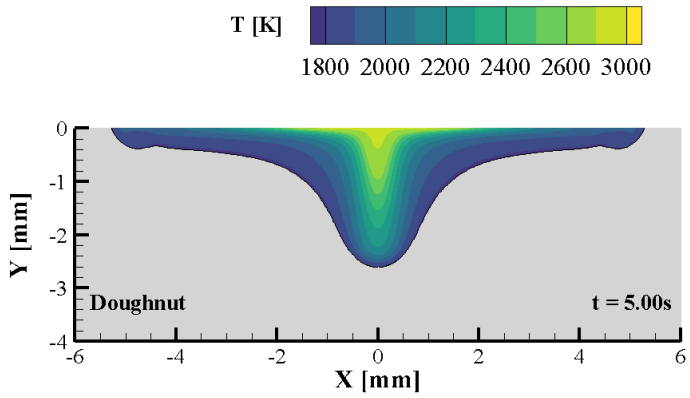

(c) Temperature distribution

Figure 6.30: Simulation of 20 ppm doughnut weld pool.

Figure 6.31 gives a more detailed picture of the difference between the 20 ppm sulfur concentration weld pool shape and 150 ppm sulfur concentration weld pool shape.

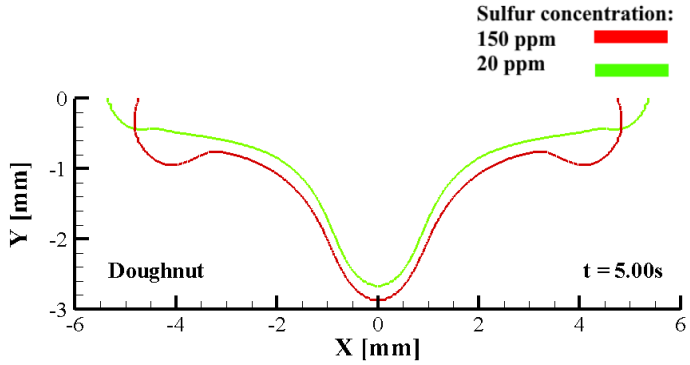

Figure 6.31: The weld pool shape of a 20 and 150 ppm sulfur concentration. In this simulation a doughnut power-density distribution is used to irradiate the SS304 for 5 s.

The figure shows that the weld pool with a 20 ppm sulfur concentration is wider, the difference is 0.6 mm. But it is also shallower, by 0.2 mm. The doughnut weld pool is the only weld pool which became significantly shallower by the use of a lower sulfur concentration. Figure 6.32 shows the development of the width and depth of the weld pool in detail.

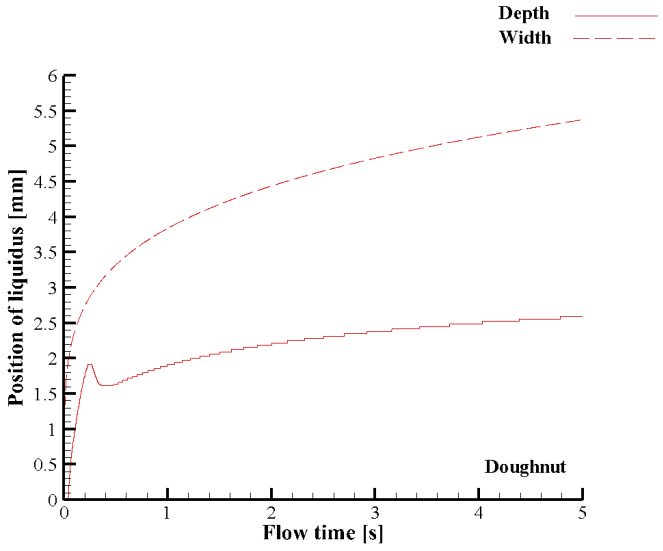

Figure 6.32: The development of the depth and the width of the weld pool when using a doughnut power-density distribution.

There is again a 0.3 mm drop in the depth of the weld pool between 0.25 s and 0.5 s, just as is the case in the 150 ppm sulfur concentration welding case. The aspect ratio has again been calculated and a graph of it is shown in figure 6.33.

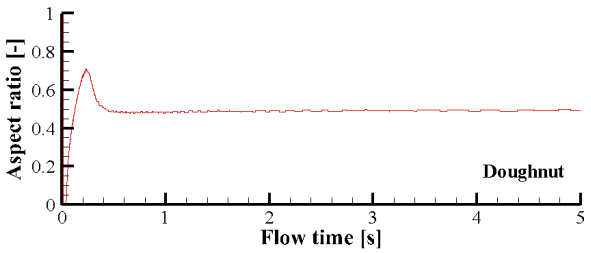

Figure 6.33: Graph showing the development of the aspect ratio for a doughnut power-density distribution using a sulfur concentration of 20 ppm.

The figure shows that the sulfur concentration has a large influence on the aspect ratio of the doughnut weld pool, difference is around 0.1. This would suggest that the sulfur concentration effects the doughnut weld pool the most.

Figure 6.34 gives a complete overview of how the 20 ppm sulfur concentration weld pool shapes compare to each other. Figure 6.34 shows that the Gaussian and top-hat weld pools are quite similar. But the top-hat weld pool is 0.5 mm wider and 0.3 mm deeper in the middle. The figure shows that the doughnut weld pool is a lot deeper than the top-hat and Gaussian weld pools. The 20 ppm doughnut weld pool is three times as deep as the Gaussian weld pool.

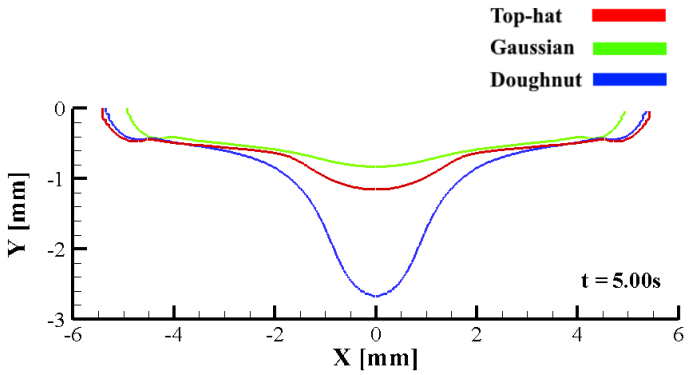

Figure 6.34: Simulation of the melting of weld pool with a 20 ppm sulfur concentration. The weld pool shape, using different laser density distributions, at 5 s.

7. Closure

7.1 Conclusions

The major goal of the present work was to create welding cases with various laser power-density distributions. These cases were tested using the solid-liquid model. The main question that had to be answered was: What are the effects of laser power-density distribution on heat and fluid flow in molten metal melting pools? In order to answer this question first an understanding of the already known physics regarding welding and various laser power-density distributions had to be obtained, this was done in chapter 2. This knowledge was used to write the methodology in chapter 3. All of this was combined in chapter 6 where the validation cases and the simulations for this thesis were shown.

It was shown that the different laser power-density distributions created slightly different weld pools when the fluid flow was disabled. The difference between the weld pools was maximally 0.15 mm in depth and 0.5 mm in width. These simulations are there to show how important the fluid flow is in the problem. In this case the doughnut power-density distribution created the widest and shallowest weld pool, but when fluid flow was enabled this power-density distribution led to the deepest weld pool by far.

The assumption in which was stated that the buoyancy force could be neglected has been tested for the top-hat power-density distribution. The weld pool shapes differed maximally 10 µm from each other. The difference was even smaller in the middle of the weld pool where the difference was around 100 nm. This result supports the assumption that the buoyancy force can be neglected in the solid-liquid model. Noteworthy is the fact that the maximum temperature was 100 K lower in the case where buoyancy force was enabled.

The case where heat loss through radiation was neglected was examined. The weld pool without heat loss through radiation was a bit wider, maximally 60 µm. The difference in the depth of the weld pools is even smaller, around 1 µm. The calculation of the comparison of the total heat loss with the heat input from the laser showed that the total heat losses are around 2% of the heat input from the laser. To conclude, including heat loss through radiation in the model does create a smaller weld pool but the differences are so small that these are negligible.

The simulations showed that the use of various laser power-density distributions have a significant influence on the weld pool shape. Specifically the doughnut distribution had a considerable impact on the shape of the weld pool. Due to the fact that extra vortices were created in the fluid flow. The doughnut power-density distribution created a weld pool which was around three times as deep than the weld pool created by the Gaussian and top-hat power-density distribution. The

top-hat power-density distribution created the widest weld pool. In the simulations, the Gaussian weld pool was the shallowest and the narrowest weld pool.

It was notable that the Gaussian weld pool and the top-hat weld pool looked similar. Due to the fluid flow being in the same direction. The differences between these two weld pool shapes are relatively small in comparison to the difference with the weld pool shape of the doughnut power-density distribution. The differences between the top-hat and Gaussian weld pool using a 150 ppm sulfur concentration are 0.32 mm in depth and 0.55 mm in width. The same is true for the 20 ppm sulfur concentration case, this time the differences are 0.34 mm in depth and 0.46 mm in width.

The Péclet numbers have been calculated for each weld pool, which were all $\mathcal{O}(\mathrm{Pe}) \sim 10^2$. Meaning that heat transport by convection is more significant than heat transport by conduction. The differences between the Péclet numbers of the weld pools were quite significant, maximally a difference of 182. It was notable that the doughnut weld pool has much lower Péclet number than the top-hat and Gaussian weld pool, which were 2 or even 3 times as big. From this can be concluded that the effect of heat transport by conduction is maximized when a doughnut power-density distribution is used.

Aside from the differences in the weld pool shape, there were also differences in the maximum temperature and the distribution of the temperature. A huge difference was found in the maximum temperature of the material between the doughnut and Gaussian/top-hat power-density distribution. This difference was around 800 K when a 150 ppm sulfur concentration was used. The difference in maximum temperature between the Gaussian and doughnut power-density distribution even increased to 1000 K when a 20 ppm sulfur concentration was used. The difference in maximum temperature can be written to the fact that, in the case of the doughnut power-density distribution, the total laser power is divided over two peaks instead of over one peak.

The shapes of the weld pools were compared for a sulfur concentration of 20 ppm and 150 ppm. The lower sulfur concentration created a wider weld pool for all the laser density distributions used. But only the doughnut weld pool had a significant decrease of 0.2 mm in its depth in the middle. However the sides of the weld pool were 0.4 mm deeper for all three power-density distributions when a sulfur concentration of 150 ppm was used. The aspect ratios of the doughnut weld pool changed the most with respect to the sulfur concentration. The difference was around 0.1. This suggests that the sulfur concentration has the most influence on the doughnut weld pool.

7.2 Recommendation for future work

7.2.1 Refining the existing results

It might be an option to refine the results which are obtained in this thesis. These results have been gathered with an eye on time constraints and computing power constraints. Meaning that the simulations can still be developed further with the use of more time and/or more computing power. Furthermore, there were some assumptions made in this paper, for example that the beam radius does not change over distance and the effect of heat loss through convection being negligible. It is an option to take a deeper look into these assumptions and find out what the effect of these assumptions is on the accuracy of the model.

As already mentioned before, there was a 0.3 m drop in the depth of the liquidus between 0.25 s and 0.5 s. This phenomena was found in the numerical simulation for the doughnut power-density distribution, for both sulfur concentrations used, using the solid-liquid model. The reason for this is yet unknown, but may be found if more research is done regarding the early creation of a weld pool using the doughnut power-density distribution.

Another interesting result found was the increase in the maximum temperature for the Gaussian weld pool using a sulfur concentration of 20 ppm compared to 150 ppm. Especially because the maximum temperature for both the top-hat and doughnut power-density distribution decreased by a lower sulfur concentration. Besides, the maximum temperature also did decrease in the sulfur validation case. Maybe if different sulfur concentrations are tried an explanation can be found for this.

If these options are carried out it would allow a positive development of the present model. Which will give better overview of the effect of various laser power-density distributions on welding behaviour.

7.2.2 Expanding on the results

There are a lot of ways in which someone could expand on the research done in this thesis. First of all it is possible to look at different laser power-density distributions. This paper has only touched upon the surface of the effect of different laser power-density distributions on welding behaviour. Only three different laser power-density distributions were taken into account during this research but there are of course way more than just these three distributions.

A good expansion on the existing research would be to analyse the effect of various laser density distributions on the surface deformation. Due to time constraints it was not possible to add cases with surface deformation to this thesis. For completeness it would be nice if these simulations were done for various sulfur concentrations. It is important to note that these simulations will require a very small time step, at least 1 µs, around 100 iterations per time step and a good mesh resolution. Hence a lot of computing power is needed to run these simulations.

This thesis is mainly focused on spot welding but it is also possible to focus on different methods. Like using a moving laser source instead of a fixed heat source, or studying the effect of various laser power-density distributions on keyhole welding.

One of the largest improvements to this research would be to include the solidification process of the weld pools. This would create a completer overview of the effect of various laser power-density distributions on weld pool behaviour.

Finally, as already mentioned in section 3.6, the use of 3D modelling over 2D axisymmetric modelling will significantly increases the accuracy of the models. Due to time constraints it was chosen to not try 3D modelling in this thesis but it is an area that is suitable for further research. It would allow for a clearer view of the effect of various laser power-density distributions on welding pool behaviour.

Bibliography

[1] CT Dawes. *Laser welding: a practical guide*. Woodhead Publishing, 1st edition, 1992.

[2] Seiji Katayama. *Handbook of laser welding technologies*. Elsevier, 2013.

[3] Qiang Chen, Gildas Guillemot, Charles-André Gandin, and Michel Bellet. Numerical modelling of the impact of energy distribution and marangoni surface tension on track shape in selective laser melting of ceramic material. *Additive Manufacturing*, 21:713–723, 2018.

[4] Beekers J.P.A. *Numerical modeling of heat transfer and fluid flow in welding with a moving heat source*. Bachelor's thesis, Delft University of Technology, 2014.

[5] Dongkyoung Lee and Jyotirmoy Mazumder. Effects of momentum transfer on sizing of current collectors for lithium-ion batteries during laser cutting. *Optics & Laser Technology*, 99:315–325, 2018.

[6] K Kheloufi, EH Amara, and A Benzaoui. Optimization of the laser cutting process in relation to maximum cutting speed using numerical modelling. *Lasers in Engineering (Old City Publishing)*, 38, 2017.

[7] JL Tan, C Tang, and CH Wong. Study and modeling of melt pool evolution in selective laser melting process of ss316l. *MRS Communications*, 8(3):1178–1183, 2018.

[8] CX Zhao, C Kwakernaak, Y Pan, IM Richardson, Z Saldi, S Kenjeres, and CR Kleijn. The effect of oxygen on transitional marangoni flow in laser spot welding. *Acta Materialia*, 58(19): 6345–6357, 2010.

[9] Jae-Hyuck Yoo, Jung Bin In, Cheng Zheng, Ioanna Sakellari, Rajesh N Raman, Manyalibo J Matthews, Selim Elhadj, and Costas P Grigoropoulos. Directed dewetting of amorphous silicon film by a donut-shaped laser pulse. *Nanotechnology*, 26(16):165303, 2015.

[10] Zhiyong Li, Gang Yu, Xiuli He, Shaoxia Li, Chongxin Tian, and Binxin Dong. Analysis of surface tension driven flow and solidification behavior in laser linear welding of stainless steel. *Optics & Laser Technology*, page 105914, 2019.

[11] Tarasankar DebRoy and SA David. Physical processes in fusion welding. *Reviews of modern physics*, 67(1):85, 1995.

[12] JF Lancaster. The physics of fusion welding. part 1: The electric arc in welding. In *IEE Proceedings B (Electric Power Applications)*, volume 134, pages 233–254. IET, 1987.

[13] Z.S. Saldi. *Marangoni driven free surface flows in liquid weld pools*. PhD thesis, Delft University of Technology, 2012.

[14] GM Oreper and J Szekely. Heat-and fluid-flow phenomena in weld pools. *Journal of Fluid Mechanics*, 147:53–79, 1984.

[15] CX Zhao, Volkert van Steijn, Ian M Richardson, Chris R Kleijn, Sasa Kenjeres, and Z Saldi. Unsteady interfacial phenomena during inward weld pool flow with an active surface oxide. *Science and Technology of Welding and Joining*, 14(2):132–140, 2009.

[16] D Delapp, G Cook, A Strauss, and W Hofmeister. Quantitative observations of surface flow and solidification on autogenous gta weld pools. 2005.

[17] P Henrikson. *Visualization of weld pool surface flow during TIG welding on stainless steel 316L plates*. na, 2005.

[18] Masami Mizutani, Seiji Katayama, and Akira Matsunawa. Observation of molten metal behavior during laser irradiation: basic experiment to understand laser welding phenomena. In *First International Symposium on High-Power Laser Macroprocessing*, volume 4831, pages 208–213. International Society for Optics and Photonics, 2003.

[19] Yasuaki Naito, Masami Mizutani, and Seiji Katayama. Effect of oxygen in ambient atmosphere on penetration characteristics in single yttrium–aluminum–garnet laser and hybrid welding. *Journal of laser applications*, 18(1):21–27, 2006.

[20] S Katayama, N Seto, M Mizutani, and A Matsunawa. X-ray transmission in-situ observation of fluid flow inside molten pool during tig arc welding of stainless steel. *Transactions of the JWRI(Japan)*, 30:487–492, 2000.

[21] ZS Saldi, A Kidess, S Kenjereš, C Zhao, IM Richardson, and CR Kleijn. Effect of enhanced heat and mass transport and flow reversal during cool down on weld pool shapes in laser spot welding of steel. *International Journal of Heat and Mass Transfer*, 66:879–888, 2013.

[22] T Chande and J Mazumder. Two-dimensional, transient model for mass transport in laser surface alloying. *Journal of applied physics*, 57(6):2226–2232, 1985.

[23] Cholik Chan, J Mazumder, and MM Chen. A two-dimensional transient model for convection in laser melted pool. *Metallurgical Transactions A*, 15(12):2175–2184, 1984.

[24] W Pitscheneder, Tarasankar Debroy, K Mundra, and R Ebner. Role of sulfur and processing variables on the temporal evolution of weld pool geometry during multikilowatt laser beam welding of steels. *Welding Journal (Miami, Fla)*, 75(3), 1996.

[25] S Mishra, TJ Lienert, MQ Johnson, and Tarasankar DebRoy. An experimental and theoretical study of gas tungsten arc welding of stainless steel plates with different sulfur concentrations. *Acta Materialia*, 56(9):2133–2146, 2008.

[26] L Han and FW Liou. Numerical investigation of the influence of laser beam mode on melt pool. *International journal of heat and mass transfer*, 47(19-20):4385–4402, 2004.

[27] Karim Kheloufi, El Hachemi Amara, and Ahmed Benzaoui. Numerical simulation of transient three-dimensional temperature and kerf formation in laser fusion cutting. *Journal of Heat Transfer*, 137(11), 2015.

[28] A Paul and Tarasankar Debroy. Free surface flow and heat transfer in conduction mode laser welding. *Metallurgical Transactions B*, 19(6):851–858, 1988.

[29] ME Thompson and J Szekely. The transient behavior of weldpools with a deformed free surface. *International journal of heat and mass transfer*, 32(6):1007–1019, 1989.

[30] P Sahoo, Tarasankar Debroy, and MJ McNallan. Surface tension of binary metal—surface active solute systems under conditions relevant to welding metallurgy. *Metallurgical transactions B*, 19(3):483–491, 1988.

[31] Vitaliy Pavlyk and Ulrich Dilthey. Simulation of weld solidification microstructure and its coupling to the macroscopic heat and fluid flow modelling. *Modelling and Simulation in Materials Science and Engineering*, 12(1):S33, 2003.

[32] Xiaofang Xu, Xiaohan Yang, Jingbo Li, Sen Pan, Yong Bi, and Yongfeng Gao. Influence of laser energy distribution on laser surface microstructure processing. *Optik*, 199:163244, 2019.

[33] Marti Duocastella and Craig B Arnold. Bessel and annular beams for materials processing. *Laser & Photonics Reviews*, 6(5):607–621, 2012.

[34] Jiazhu Wu, Haiying Wei, Fengbo Yuan, Penghui Zhao, and Yi Zhang. Effect of beam profile on heat and mass transfer in filler powder laser welding. *Journal of Materials Processing Technology*, 258:47–57, 2018.

[35] Jesper Sundqvist, AFH Kaplan, L Shachaf, A Brodsky, C Kong, Jon Blackburn, Eurico Assuncao, and Luisa Quintino. Numerical optimization approaches of single-pulse conduction laser welding by beam shape tailoring. *Optics and Lasers in Engineering*, 79:48–54, 2016.

[36] Shakeel Safdar, Lin Li, and MA Sheikh. Numerical analysis of the effects of non-conventional laser beam geometries during laser melting of metallic materials. *Journal of physics d: applied physics*, 40(2):593, 2007.

[37] MA Sheikh and L Li. Understanding the effect of non-conventional laser beam geometry on material processing by finite-element modelling. *Proceedings of the Institution of Mechanical Engineers, Part C: Journal of Mechanical Engineering Science*, 224(5):1061–1072, 2010.

[38] AV Oppenheim, AS Willsky, and SH Nawab. Signals & systems: Pearson new international edition, 2/e. *Harlow, Essex, England: Pearson Education Limited*, 2013.

[39] Massimo Santarsiero and Riccardo Borghi. Correspondence between super-gaussian and flattened gaussian beams. *JOSA A*, 16(1):188–190, 1999.

[40] Yajun Li. Light beams with flat-topped profiles. *Optics letters*, 27(12):1007–1009, 2002.

[41] J. R. A. Pearson. On convection cells induced by surface tension. *Journal of Fluid Mechanics*, 4(5):489–500, 1958. doi: 10.1017/S0022112058000616.

[42] Warmoeskerken M.M.C.G. Janssen L.P.B.M. *Transport phenomena data companion*. VSSD, 3rd edition, 2006.

[43] C Limmaneevichitr and S Kou. Experiments to simulate effect of marangoni convection on weld pool shape. *WELDING JOURNAL-NEW YORK-*, 79(8):231–S, 2000.

[44] M Reza Aboutalebi, M Hasan, and RIL Guthrie. Numerical study of coupled turbulent flow and solidification for steel slab casters. *Numerical Heat Transfer. Part A, Applications*, 28(3), 1995.

[45] Lightfoot E.N. Bird R.B., Stewart W.E. *Transport phenomena.* John Wiley Sons Inc., 2nd edition, 2002.

[46] Y Sharir, A Grill, and J Pelleg. Computation of temperatures in thin tantalum sheet welding. *Metallurgical Transactions B*, 11(2):257–265, 1980.

[47] AD Brent, Vaughan R Voller, and KTJ Reid. Enthalpy-porosity technique for modeling convection-diffusion phase change: application to the melting of a pure metal. *Numerical Heat Transfer, Part A Applications*, 13(3):297–318, 1988.

[48] Mudde R. Van den Akker H. *Fysische transportverschijnselen: denken in balansen.* Delft acedemic press, 4th edition, 2014.

[49] P Ferro, H Porzner, A Tiziani, and F Bonollo. The influence of phase transformations on residual stresses induced by the welding process—3d and 2d numerical models. *Modelling and Simulation in Materials Science and Engineering*, 14(2):117, 2006.

[50] A Kidess. *Multiscale modeling of mesoscale phenomena in weld pools.* PhD thesis, Delft University of Technology, 2016.

[51] Amin Ebrahimi, Chris R Kleijn, and Ian M Richardson. Sensitivity of numerical predictions to the permeability coefficient in simulations of melting and solidification using the enthalpy-porosity method. *Energies*, 12(22):4360, 2019.

[52] Vaughan R Voller and C Prakash. A fixed grid numerical modelling methodology for convection-diffusion mushy region phase-change problems. *International Journal of Heat and Mass Transfer*, 30(8):1709–1719, 1987.

[53] ANSYS®. *Student 2019 R3.* ANSYS, 2016.

[54] Raad I Issa. Solution of the implicitly discretised fluid flow equations by operator-splitting. *Journal of computational physics*, 62(1):40–65, 1986.

[55] JP Van Doormaal and GD Raithby. Enhancements of the simple method for predicting incompressible fluid flows. *Numerical heat transfer*, 7(2):147–163, 1984.

[56] Vaughan R Voller and CR Swaminathan. Eral source-based method for solidification phase change. *Numerical Heat Transfer, Part B Fundamentals*, 19(2):175–189, 1991.

[57] Vaughan R Voller. Development and application of a heat balance integral method for analysis of metallurgical solidification. *Applied mathematical modelling*, 13(1):3–11, 1989.

[58] Chie Gau and R Viskanta. Melting and solidification of a pure metal on a vertical wall. *Journal of Heat Transfer*, 108(1):174–181, 1986.

[59] Noureddine Hannoun, Vasilios Alexiades, and Tsun Zee Mai. Resolving the controversy over tin and gallium melting in a rectangular cavity heated from the side. *Numerical Heat Transfer: Part B: Fundamentals*, 44(3):253–276, 2003.

[60] S Patel, A Aggrawal, A Kumar, and VK Jain. High-speed conduction-mode micro-laser welding of thin ss-304. *Advances in Micro and Nano Manufacturing and Surface Engineering: Proceedings of AIMTDR 2018*, page 153, 2019.

[61] HG Kraus. Experimental measurement of stationary ss 304, ss 316 l and 8630 gta weld pool surface temperatures. *Weld. J.*, 68(7):269, 1989.

[62] K Mundra, T Debroy, T Zacharia, and S David. Role of thermophysical properties in weld pool modeling. *Welding Journal(USA)*, 71(9):313, 1992.

Acknowledgements

This thesis is not only my accomplishment but the combined effort of several people who helped me to complete it. First of all, I want to thank my daily supervisor Amin Ebrahimi. He helped me to understand the physics behind weld pools, how to create simulations and especially how to write a good report. I could always ask questions and I learned a lot from our meetings. His critical reviews and suggestions allowed me to refine my work. Above all he has a passionate approach to practice science which is contagious.

I also want to thank my responsible supervisor Sasa Kenjeres for helping me create this thesis. His enthusiasm during our meetings always gave me a boost in motivation. When I asked for help he always tried to find a way to help me.

I want to thank everyone in the TP group for sharing their resources with me and organizing fun activities. Besides, I want to thank Sandra Paffen for helping me get the resources I needed in order to complete this thesis.

Finally, I would like to thank my parents for all the help they offered while working this thesis. My mother has read this thesis more times than I can count and helped me a lot with the spelling and grammar, as that is definitely not my best feature. My father offered all his support and he tried to help me wherever possible.